












Evidence for the gravity-driven and magnetically-regularized gas flows feeding the massive protostellar cluster in Cep A

Panigrahy Sandhyarani ¹, Chakali Eswaraiah ^{1*}, Enrique Vázquez-Semadeni ², Gilberto C. Gómez ², Travis J. Thieme ³, Manash R. Samal ⁴, Di Li ⁵, Jia-Wei Wang ^{3,6}, Shih-Ping Lai ⁷, Wen-Ping Chen ⁸, and D. K. Ojha ⁹

¹Department of Physics, Indian Institute of Science Education and Research Tirupati, Yerpedu, Tirupati - 517619, Andhra Pradesh, India
sandhyaranipanigrahy@students.iisertirupati.ac.in, eswaraihc@labs.iisertirupati.ac.in

²Instituto de Radioastronomía y Astrofísica, Universidad Nacional Autónoma de México, 58090 Morelia, Michoacán, Mexico

³Academia Sinica Institute of Astronomy & Astrophysics, 11F of Astronomy-Mathematics Building, AS/NTU, No.1, Section 4, Roosevelt Road, Taipei 10617, Taiwan

⁴Physical Research Laboratory (PRL), Navrangpura, Ahmedabad 380 009, Gujarat, India

⁵CAS Key Laboratory of FAST, National Astronomical Observatories, Chinese Academy of Sciences, Datun Road, Chaoyang District, Beijing 100101, People's Republic of China

⁶East Asian Observatory, 660 N. Aóhōkū Place, University Park, Hilo, HI 96720, USA

⁷Institute of Astronomy and Department of Physics, National Tsing Hua University, Hsinchu 30013, Taiwan

⁸Institute of Astronomy, National Central University, Taoyuan 32001, Taiwan

⁹Department of Astronomy and Astrophysics, Tata Institute of Fundamental Research, Mumbai 400005, India

The hierarchical interplay among gravity, magnetic fields, and turbulent gas flows in delivering the necessary material to form massive protostellar clusters remains enigmatic. We have performed high-resolution (beam size ~ 14 arcsec $\simeq 0.05$ pc at a distance 725 pc) 850 μm dust polarization and C^{18}O molecular line observations of Cepheus A (Cep A), the second closest massive star-forming region, using the 15-meter James Clerk Maxwell Telescope (JCMT) along with the SCUBA-2/POL-2 and HARP instruments. Our key analyses reveal that (i) morphologically, all three fields—gravitational (G), magnetic (B), and kinetic (K) fields—are aligned with each other, and (ii) energetically, they exhibit a hierarchical relationship with gravitational (E_G) > magnetic (E_B) > kinetic (E_K). Gravity dominates in Cep A clump and, as a *primary active player*, dictates the other two agents. Consequently, gravity plays two active roles: (i) induces gas flows and (ii) drags B-field lines toward the gravitational trough. Since magnetic energy dominates kinetic energy, $E_B > E_K$, the “dragged-in” B-field as a *secondary active player* can mitigate turbulence and instabilities, thereby regularizing gas flows into a more ordered configuration. At the ~ 0.60 pc clump scale, these flows deliver material at a substantially high rate of \sim

$2.1 \times 10^{-4} M_{\odot} \text{ yr}^{-1}$ toward the cluster center. Our study, for the first time, presents new insights into how B-fields and turbulent gas flows *passively* assist the *active* role of gravity in the formation of a protostellar cluster, contrasting with the standard notion that these agents primarily oppose gravitational collapse. The ~ 0.6 pc clump-scale B-field, oriented northeast-southwest with a mean position angle of $\sim 45^{\circ}$, shows a coherent alignment with B-fields at the ~ 5 pc cloud, ~ 0.05 pc core, and ~ 1000 AU disc scales.

Massive stars ($M > 8 M_{\odot}$) play a significant role in the evolution and enrichment of the interstellar medium (ISM) within their host galaxy^{1,2}. Despite their pivotal importance, the formation process of high-mass stars remains a puzzle awaiting a comprehensive unraveling. Over the past decade, Hub-Filament Systems (HFSs) have emerged as prominent sites for high-mass star formation^{3–9}. Converging flows along the filaments supply gas towards the hub, where fragmented massive cores are believed to compete for material from the gas reservoir. Protostars near the gravitational potential center can accrete matter at higher rates, leading to the formation of massive stars^{10,11}. It has now been well established that the collaborative interplay among the key parameters –gravity, turbulence, and the B-field – is pivotal in governing the formation and fragmentation of clouds into filaments, clumps, and cores¹ and the subsequent collapse of cores to form stars^{13–16}.

Although various properties of HFSs have been investigated using dust continuum and spectral line data^{17,18}, studies focusing on their B-fields are relatively limited^{19–22}. Previous studies on B-fields in interstellar filaments based on optical, near-infrared, and sub-millimeter polarization observations revealed that the B-fields tend to align parallel to the filament in diffuse regions and perpendicular to the filament’s spine in denser regions as revealed by observational studies^{23–25} and simulations^{26,27}. The morphological correlation between filaments and B-fields may vary based on the column densities along or across the filaments^{28–30}, such that the role of the B-field may evolve locally depending on the dominance of one agent on the other. For instance, in massive star-forming regions, the gravitational force is the most dominating force^{31–33}. In addition, these regions are also magnetically predominant with strengths of a few mG (0.1 - 6 mG) at clump and core scale^{34–36} to a few 100s of mG at the disc scale³⁷. While gravity primarily drives the collapse of the clouds, the role of B-field – especially whether it controls the gravitational contraction and collapse *actively* or getting shaped by gravity *passively* – is unclear. It has been shown that gravitational collapse also induces turbulent gas flows³⁸. Since turbulence and B-fields are coupled, their combined impact depends on which factor is dominant. Therefore, detailed investigations into the local morphological variations of B-fields, gravity, and turbulence, along with their interactions at the clump scale, are limited, leaving the hierarchical role of each factor unresolved.

In this study, we investigate the second nearest (~ 725 pc³⁹) massive star-forming clump ($1200 M_{\odot}$ ⁴⁰) Cepheus A (Cep A) located in the Cepheus OB3 cloud complex. Cep A hosts an early-type massive protostar (spectral type $\sim B0.5$, and mass $\sim 15M_{\odot}$) known as Cep A-HW2. The core hosting HW2 is surrounded by a cluster of far-infrared (FIR) sources, indicating the formation of a massive protostellar cluster⁴¹. The protostar Cep A-HW2 is in an early stage of evolution, characterized by active jets, outflows, and ongoing accretion activity^{42,43}. Despite this, it has not yet disrupted the entire parental clump, Cep A, as evidenced by the dust continuum emission map (Figure 1), and thus retains its pristine physical conditions. These characteristics make Cep A an ideal laboratory for examining the detailed structure of B-fields and investigating their role alongside gravity and turbulence in the protostellar cluster environment.

We have performed sensitive sub-millimeter dust polarimetric observations at $850 \mu\text{m}$ to-

¹we adopt the dimensions and properties of cloud, clump, and core as per Zhang et al.¹²

wards Cep A using the Submillimetre Common User Bolometer Array (SCUBA-2) in conjunction with the polarimeter (POL-2) on the James Clerk Maxwell Telescope (JCMT) in Hawaii. The B-fields were traced using JCMT but in combination with an old camera, SCUBA, plus polarimeter, POL, (SCUPOL⁴⁵), however, they were limited in both low- and high-density regions^{46,47}. Our new observations with POL-2 have delineated the detailed B-field morphology over the scales of $\sim 0.05 - 0.60$ pc of Cep A clump as shown in Figure 1 (Refer to **Methods** for more details). The overall B-field structure is quite organized on a larger scale. However, within each of its portions, the orientation of the B-field varies smoothly from large to small scales, consistently pointing toward the densest region of the clump and exhibiting a converging feature towards the center.

Based on our analysis below, Cep A is a promising candidate for HFS. The filamentary structures at the cloud scale are evident in the Herschel 250 μm data (see the left panel of Extended Data Figure 1). Using the **FILFINDER** algorithm, we identified these gas structures in the ^{13}CO ($J = 1-0$) spectral data from the Purple Mountain Observatory’s (PMO) Milky Way Imaging Scroll Painting (MWISP) survey. To investigate the gas kinematics, we extracted velocity profiles along the filaments, which revealed a clear velocity gradient from the outskirts towards the hub on the cloud scale (Extended Data Figure 2). Additionally, we analyzed C^{18}O ($J = 3-2$) data on the clump scale obtained through the JCMT’s Heterodyne Array Receiver Program (HARP). The velocity gradients extracted along the four cuts, as shown in the bottom panel of Extended Data Figure 2, indicate an inward gas motion. The gas kinematics of the identified structures indicate a global convergence of gas movements toward the center at both the cloud and clump scales. To trace and investigate the infalling gas structures in Cep A, we analyse the HARP C^{18}O spectral cube with velocity channels ranging from -12.5 to -8 km/s that are free from the outflows⁴². We employed **astrodendro** algorithm on the extracted C^{18}O spectral cube, which discloses a prominent gas structure with four extended leaf structures (shown in Extended Data Figure 3 and 4).

Cep A hosts an active and energetic outflow emanated from the HW2, which is well-traced by shock-excited $\text{H}_2/2.12$ μm emission (Extended data Figure 6). To investigate the relation between outflows and the B-field, an offset map is made by calculating the difference between the mean position angle of outflows in a given region (determined by the average direction of shock fronts⁴²; **Methods**) and the B-field (Extended Data Figure 7). Smaller offset angles, indicated with red pixels, suggest either the outflow has shaped B-fields in the east-west regions or the B-field has guided the outflows. The dominance of one on the other factor can be determined by comparing their energies at different scales. At the disc scale, the Zeeman effect of H_2O and OH masers yielded a few 10s to several 100s of mG of B-field strength in the vicinity of HW2 disc³⁷. These B-fields are dynamically strong enough to launch the outflows from the HW2 protostar⁴⁸⁻⁵⁰. In addition, B-fields with strengths of few to several mG at the clump scale (present work; see Extended data Figure 8; see also Curran & Chrysostomou³⁴) as well as at core scale³⁶, could still guide the pc-scale outflows. To strengthen this evidence, we evaluated the outflow energies of the blue- and red-shifted components as 9.5×10^{38} and 8.9×10^{38} erg, respectively (**Methods**). Additionally, we calculated the average magnetic energy (E_B) to be 1.1×10^{47} erg, indicating that the B-fields are sufficiently strong to guide the outflows in the east-west direction.

We focus on regions unaffected by outflows to analyze the interplay between B-field, gravity, and turbulence to understand their relative importance in the Cep A clump. To examine the significance of the B-field relative to gravity, we produce the global gravitational field vectors at each pixel of the dust emission map (For details, refer **Methods**). Figure 2(a) shows that the projected vectors point towards the center. To understand the relative orientation of B-fields

and gravity, we produced the absolute offset angle map by taking the difference between the position angles of the gravitational field vector and the B-field position angle (PA) (shown in Figure 2(b)). The smaller offset angles in the North (N) and South (S) regions marked as red pixels reveal that the gravity and B-field are well-aligned with each other.

To quantitatively assess which factor, gravity or the B-field, is dominant in Cep A, we have employed the term ‘ $\sin \omega$ ’ through the Magnetohydrodynamic (MHD) force equation⁵¹ (Methods). Here, ω is the offset angle between gravitational field vector and B-field PA shown (Figure 2(b)). For the local collapse to occur, the gravitational force must exceed the magnetic force at a specific location, causing the B-field line to bend in response to gravity. This scenario results in a close alignment between the B-field and gravity and hence smaller $\sin \omega$ values, which is true in the N and S regions because a majority of the blue pixels were found (Figure 2(c)). Therefore, $\sin \omega$ analysis hints at how effectively gravity shapes and aligns the field lines in the N and S regions.

To quantify the local influence of B-field relative to other forces at play, such as gravity and any other pressure gradient (resultant of thermal/kinetic and non-thermal/turbulent gas pressures), we calculated the parameter Σ_B ^{51,52} (Figure 2(d)). This parameter is equivalent to $F_B/(F_G + F_P)$, where F_B is the magnetic force, F_G is the gravitational force, and F_P is the pressure force. This force ratio is calculated by taking the ratio $\sin \psi / \cos \alpha$, where ψ represents the offset angle between the gravitational field vector and the intensity gradient, and α is the angle between the B-field and the intensity gradient. In the N and S region, where the value of $\sin \omega$ is lower, the Σ_B values are also less than 1, indicating that gravity dominates over the magnetic field support, pulling the B-fields toward the gravitational trough. The consequence of this scenario would be that gravity would exert a maximum acceleration on the gas, inducing and directing the gas flow (as evident from Extended Data Figure 2) along the gravitational pull. Under the assumption of flux-freezing^{53–55}, this process also drags B-field lines coupled with the gas flows. We calculated the B-field strength using both the Davis-Chandrasekhar-Fermi (DCF) method^{56,57} with various correction factors and the recently introduced Sklidis-Tassis (ST) method⁵⁸. Since the DCF method tends to overestimate the B-field strength, we opted to use the ST method in our analysis, as it incorporates the incompressible modes of turbulence^{16,59} (for more details, refer Methods section). To elucidate further, we also estimated the gravitational (E_G), magnetic (E_B), and kinetic (E_K) energies in the clump as a function of radial distance from the center (Figure 3, Methods). Our analysis shows that E_G is predominant throughout the clump, with an average energy of 1.1×10^{47} erg. Interestingly, the dominance of E_B over E_K (as seen in Figure 3) suggests that the higher B-field strength may suppress turbulence and inhibit secondary fragmentation along the conveyor-like flow. This is because the magnetic tension tends to dampen the dynamical instabilities and hence reduces the turbulence along the converging flows^{60,61}, which makes the flow more ordered. In addition, while gas moves more freely along the strong field lines, their motion will be hindered in the direction perpendicular to the field lines^{62–69}. Thus, the B-fields can be envisioned as channels directing water to a lake, providing a pathway for the inflowing material. *Indeed, gravity and B-field act hand-in-hand such that gravity induces gas flows and also pulls field lines, while the B-field regularizes these flows along the field lines towards the trough, aiding gravity’s effort.*

We strengthen our findings of magnetically-regularized gas flows along the NE and SW orientation based on the comparison of B-fields at various scales – probed by *Planck* in the cloud, JCMT SCUBA-2/POL-2 in the clump (present work), SMA (Submillimeter Array) in the core³⁶ and MERLIN (Multi-Element Radio Linked Interferometer Network) in the vicinity of circumstellar disc⁷⁰ as shown in Figure 4. At the cloud scale, the B-field appears uniformly oriented nearly along the SouthEast-NorthWest (SE-NW) orientation with $108 \pm 14^\circ$ from North

(Figure 4(a)). However, close to the NE portion of the cloud, they tend to be dragged towards the hub with a position angle of $39.2 \pm 13.6^\circ$ along the filament F1 towards the hub (Figure 4(a); see also Extended Data Figure 1(b)). A clear velocity gradient along the filament F1 towards the hub is also evident (Second row in Extended Data Figure 2). At the clump scale, B-fields appear organized; nonetheless, they are dragged towards the center, thereby aligned along the direction of gas structures, and towards the center, B-fields exhibit a twisted pattern (Figure 4(b); also see Extended Data Figure 4). At the ~ 0.005 pc core scale, the B-field is aligned with the south-west elongated tail-like structure, and they are connected smoothly to the head-like core (Figure 4(c)). A comparison of POL-2 segments with those of SMA reveals a similarity between core and clump scale B-field. At the vicinity of the circumstellar disc, the B-fields, probed using 6.7 GHz methanol maser polarization data, are oriented along NorthEast-SouthWest (NE-SW) with a mean position angle of $33.3 \pm 17.7^\circ$, which is parallel to the radio jet and perpendicular to the disc. This component of the B-field is coherent with the B-field at the clump and core scales. A toroidal B-field component is also evident as per Figure 4(d), where the B-field, initially oriented in the NE-SW, tends to be twisted along the disc. Vlemmings et al.⁷⁰, based on the relation between gas density and B-field strength show that gas collapses along the magnetic field lines, suggesting that the B-field likely regularizes accretion onto the disk around the massive protostar Cep A HW2. The histograms of B-fields across all scales, presented in Figure 5, evidence the dominant B-field component centered around 45° with orientations spanning from 150° to 180° or 0° , and to 60° . Therefore, gravity-driven and magnetically-regularized collapse in the N and S regions is evident at the clump-to-disc scale, and such an important finding is further supported by the signature of bend in the cloud-scale B-field and a similarity in the morphologies of core- and disc-scale B-fields.

To concrete our findings regarding whether the gas structures collapse under gravity, *firstly*, we compared the data points of the dendrogram structures in the position-position-velocity (PPV) space with the data points in the trajectories produced by the Cassen-Moosman-Ulrich (CMU) model^{71–73} (Figure 6; see [Methods](#) for details on the CMU model). The comparison between the CMU modeled trajectories and the observed dendrogram data in the PPV space shows a 76% match, indicating it is likely a gravitationally collapsing structure. The three-dimensional gas structure in PPV space is projected into two-dimensional position-position (PP) and position-velocity (PV) plots (middle and bottom panel of Figure 6). As shown in PP space, a close alignment between B-fields and the gas flows represented by CMU-modeled trajectories signifies a scenario where the initial B-fields could have been dragged in by gravity, consequently they tend to regulate the gas flows along the direction of gravitational pull towards the potential trough. *Secondly*, by comparing the gravity vectors with the infalling gas structures inferred by the CMU model trajectories, as shown in the middle panel of Figure 6, we conclude that the gas velocity field is also aligned along the gravity. By determining the mass of this infalling dendrogram structure to be $120 M_\odot$, we calculated the envelope infall rate as $(2.1 \pm 0.4) \times 10^{-4} M_\odot \text{ yr}^{-1}$ ([Methods](#)). This infall rate matches with the required accretion rate to overcome the radiation pressure and form massive stars^{74–77}. Such high infall rates are crucial for the growth of protostars to emerge as massive stars.

The proximity of Cep A HW2 allows us to zoom in on the clump and its fragmented sub-structures. Cep A hosts a protostellar cluster within a radius of $1''$ (725 AU). This is evidenced based on the observed three young protostars, HW2, HW3c, and HW3d, forming within a projected area of $\approx 0.6 \times 0.6''$ ($400 \times 400 \text{ AU}^2$) and three hot cores HC, HC2, and HC3^{78,79}. Of these six, HW2 stands out as the most luminous source in Cep A with $L \approx 10^4 L_\odot$, suggesting a mass equivalent to $15 M_\odot$ ⁴². Thus, we propose accretion is likely active in the hub, where the envelope is undergoing gravity-driven magnetically regulated collapse with an infall rate of (2.1

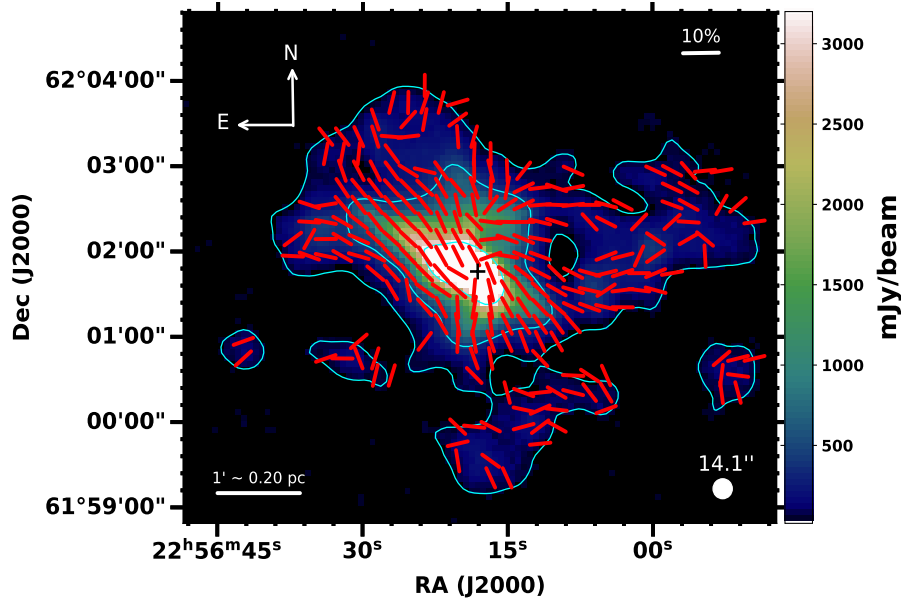


Fig. 1 | The detailed B-field geometry (red segments) of Cep A clump using JCMT SCUBA-2/POL-2 observations. All segments are depicted at equal lengths to visualize the B-field geometry better. The background image is the dust continuum map at 850 μm . The cyan contours are drawn at 32, 430, and 3000 mJy/beam. The outermost contour at 32 mJy/beam corresponds to 10σ , where $\sigma = 3.2$ mJy/beam is the rms noise in the dust continuum map. The color bar on the right denotes the intensity scale across the region. The white circle represents the beam size and the '+' sign represents the position of Cep A HW2 protostar.

$\pm 0.4) \times 10^{-4} M_{\odot} \text{ yr}^{-1}$. In the Cep A massive star-forming region, matter flows inward under gravitational influence in a magnetically-regularized conveyor belt fashion from the cloud to clump, core, and disc scale, while the mass-segregated cluster forms with the massive star at the center.

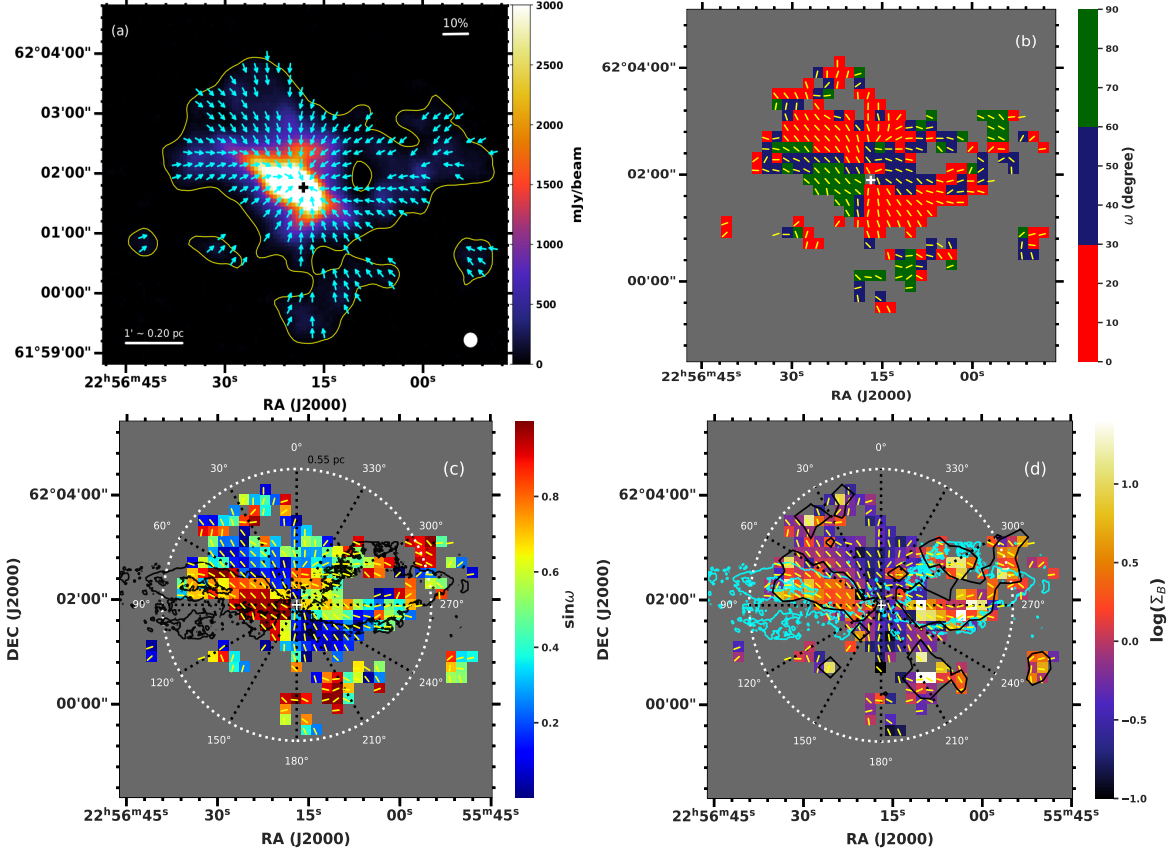


Fig. 2 | (a) The gravitational field vector map, represented by cyan vectors, overlaid on the POL-2 Stokes I map. Yellow contour corresponds to POL-2 Stokes I of 32 mJy/beam. (b) The offset angle (ω) map reveals the morphological correlation between the fields of B-field and gravity. The color bar depicts the color scheme according to different omega values. (c) Represents the $\sin \omega$ map. To identify the regions with different $\sin \omega$ values, the entire clump is depicted with an azimuthal angle $0^\circ - 360^\circ$ (white dotted circle) and radius (black dotted lines), and (d) Σ_B map in logarithmic scale with base 10. The black contour encloses pixels with $\Sigma_B > 1$. This implies that the pixels outside this contour appear blue with $\Sigma_B < 1$. The yellow segments depict the B-field orientation traced by POL-2. Black and cyan contours in panels (c) and (d) are the same, depicting the spatial distribution of H₂ 2.12 micron shocked emission of 200 mJy/beam. The pixels with smaller $\sin \omega$ and Σ_B values are evident within the azimuthal angles 330° to 30° in the north and 150° to 240° in the south (in the anticlockwise direction). The pixels distributed within these azimuthal angles have the B-field position angles lying between 150° to $180/0^\circ$, to 60° . The '+' marks the HW2 protostar in all the panels.

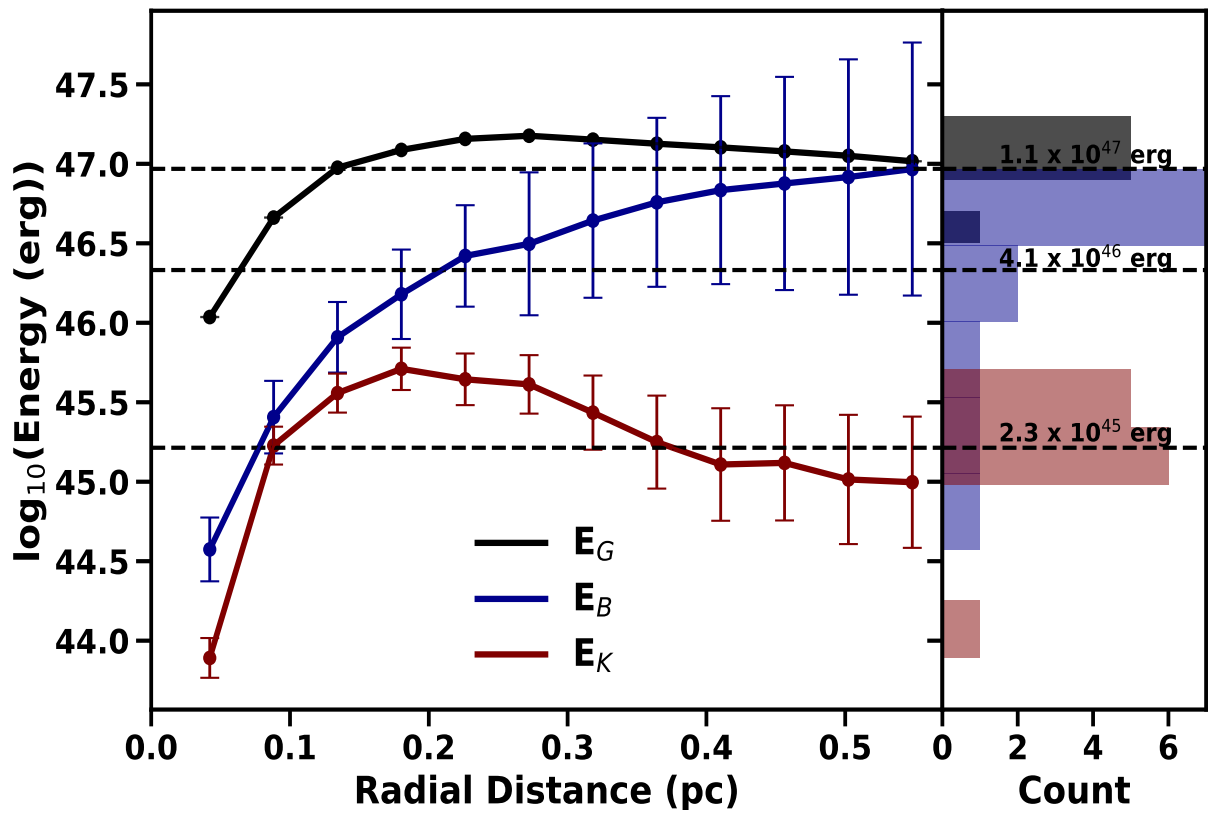


Fig. 3 | Radial distance versus gravitational (E_G), magnetic (E_B), and kinetic (E_K) energies. The histograms on the right correspond to the number distribution of energies. Horizontal dashed lines indicate the average energy values. Uncertainties in E_G are small and comparable to the size of the symbols.

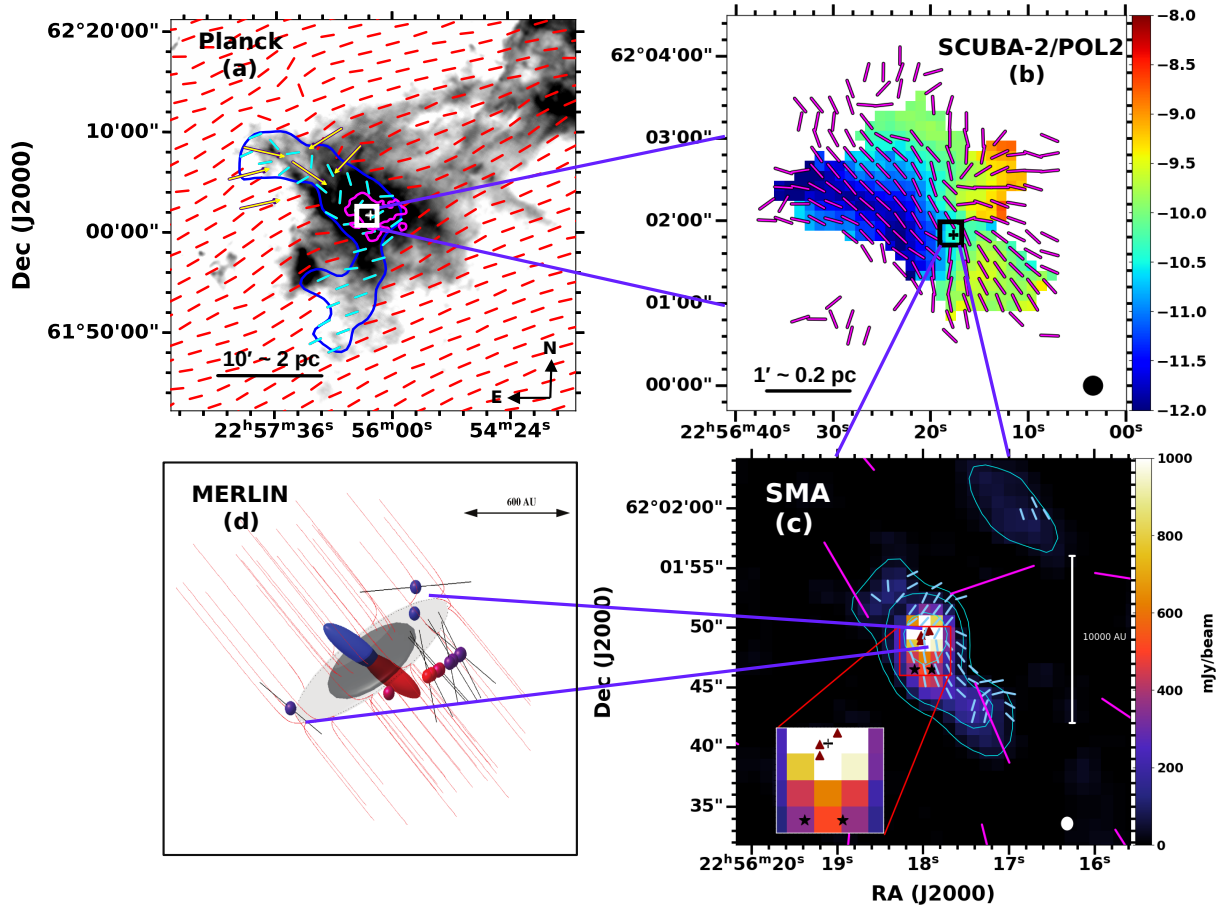


Fig. 4 | Evolution of B-field structures in the Cep A region from large-scale cloud to small-scale clump, core, and disc scale of the massive protostar Cep A HW2. (a) *Planck* 850 μm B-field segments (resolution $\sim 5'$ and pixel size $1'$) overlaid on the *Herschel*/SPIRE 250 μm map using red segments. The blue contour, drawn at 3 K km/s, traces filament F1 based on the ^{13}CO moment 0 map (see Extended Data Figure 2). The B-field segments lying within that contour are marked in cyan. The possible gravity driven bend in the B-field is shown by yellow arrows. The magenta contour represents the POL-2 dust continuum emission at 32 mJy/beam. (b) Clump-scale B-fields based on the POL-2 data are shown with magenta segments. The background image is the velocity map revealing a prominent gas structure identified via dendrogram analyses performed on the HARP C^{18}O data. (c) Core-scale B-fields based on high resolution ($\sim 3''$) observations at 875 μm ³⁶ using SMA are shown with gray segments. A few magenta segments of POL-2 are also shown for comparison. The plus and star symbols correspond to three protostars HW2 (top), HW3c (right), and HW3d (left), while the triangle symbols represent three hot cores HC (top), HC2 (middle), and HC3 (bottom)⁸⁷, and (d) B-fields in the circumstellar disc of Cep A HW2 traced by methanol maser (colored filled circles) polarization observations using the MERLIN telescope at 6.7 GHz (beam size ~ 30 mas) are shown with black segments. The thin red lines oriented in NE-SW trace the proposed B-field morphology piercing through the circumstellar disc. The panel (d) has been adapted from Vlemmings et al.⁷⁰.

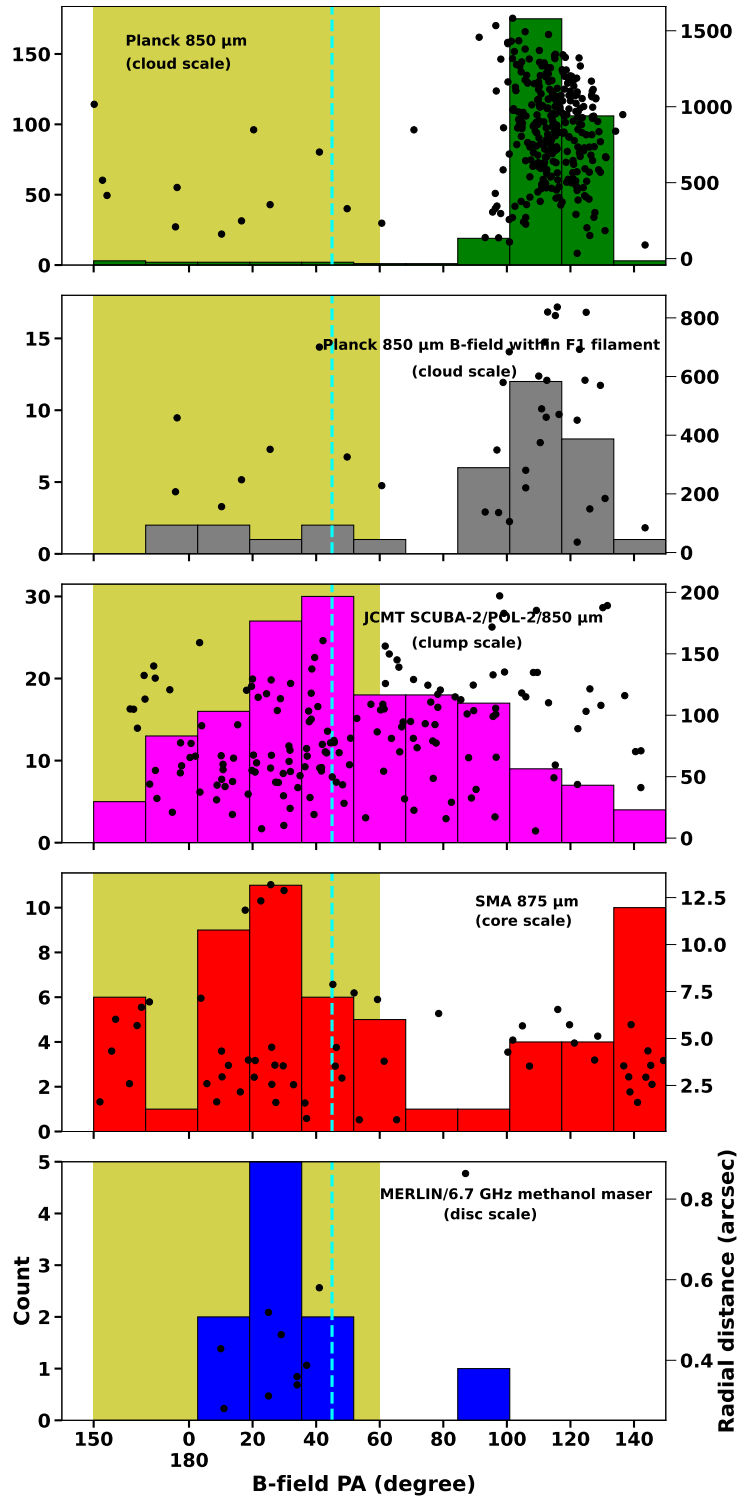


Fig. 5 | The histograms of the B-field position angles at different scales. The scatter plot represents the B-field position angles versus radial distance. The cyan dashed line drawn at $\theta = 45^\circ$ marks the position angle of the radio jet from HW2. Yellow shaded area denotes the prominent B-field angles, 150° to $180^\circ/0^\circ$, to 60° , present mainly in N and S regions Cep A (see Figure 2 for more details).

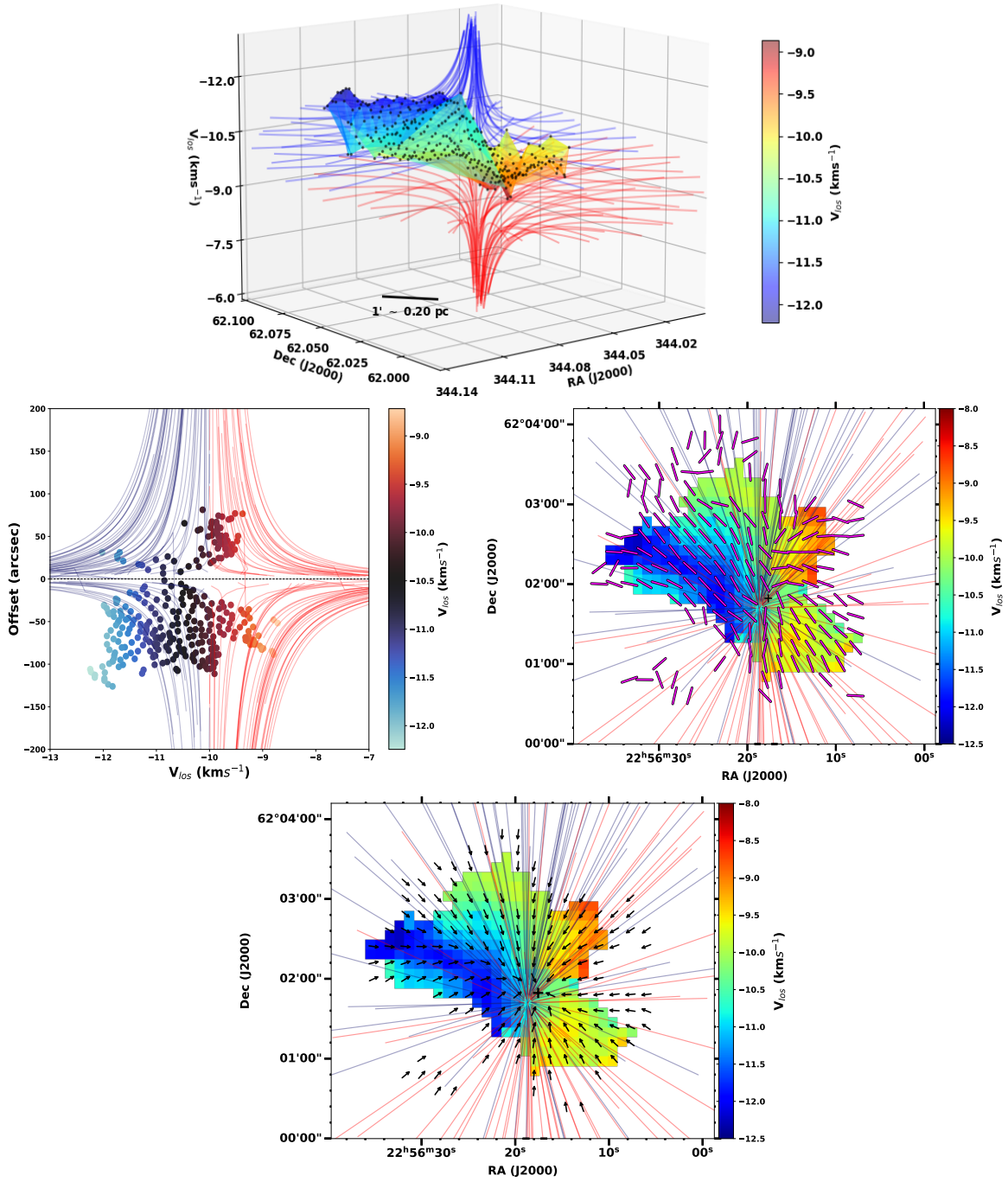


Fig. 6 | (Top): Position-Position-Velocity (PPV) data of the gas structures identified based on the dendrogram analyses on JCMT/HARP $C^{18}O$ data. The matched trajectories from the CMU model are shown as red and blue-shifted lines. (Middle left): Projected position-velocity (PV) plot showing the matched CMU modeled trajectories (blue and red lines) to the observations (scattered data). The data points extracted from dendrogram analyses are color-coded according to their velocities. (Middle right): Projected position-position (PP) plot showing matched trajectories to the data points. POL-2 B-field segments are also overlaid on them, and (Bottom): Gravitational field vectors (black vectors; same as those shown in Figure 2(a)) and CMU-modeled trajectories are overlaid on the centroid velocity (moment 1) map of the dendrogram structure. The ‘+’ sign represents the HW2 protostar.

Methods

Observations and data reduction

We carried out polarization continuum observation towards massive star-forming region Cep A with the reference position at $\alpha_{J2000.0}=22^{\text{h}}55^{\text{m}}51.44^{\text{s}}$, $\delta_{J2000.0}=62^{\circ}01'51.3''$ with SCUBA-2 POL-2 mounted on the JCMT (Project code: M19BP061; PI: Eswaraiah Chakali). SCUBA-2/POL-2 achieved a better sensitivity (~ 3.2 mJy/beam) compared to the previous generation instrument SCUBA/POL (~ 29 mJy/beam)⁴⁶. All these observations were taken in Band-2 weather conditions with opacity $\tau_{225\text{GHz}}$ span a range from 0.05 to 0.08. In this study, a single observation using the POL-2 instrument involved a 40-minute observing session employing the POL-2 DAISY scan pattern⁸⁰. JCMT has an effective beam size of $14.1''$ (~ 0.049 pc)⁸¹. The obtained data were subsequently processed through a two-step reduction procedure utilizing the `pol2map` routine, which was integrated into the Sub-Millimeter User Reduction Facility `SMURF` package of Starlink software⁸². Continuum polarisation at both 450 and 850 μm was seen concurrently. Here in this study, the 850 μm data is taken into consideration.

The C^{18}O ($J = 3-2$ transition) spectral line observations at 329.331 GHz were conducted with JCMT/HARP under the extended observing program (Project code: M22BP020; PI: Eswaraiah Chakali). These observations were performed in Band 2 weather conditions. The data reduction was carried out using the ORAC Data Reduction (ORAC-DR) pipeline and the Kernel Application Package (KAPPA⁸³) within Starlink, as detailed by Buckle et al.⁹⁰.

The ^{13}CO ($J = 1-0$ transition) molecular line observations at 110.201 GHz were observed with the 13.7-m radio telescope as a part of the Milky Way Imaging Scroll Painting (MWISP) survey, led by the Purple Mountain Observatory (PMO). These observations were done simultaneously using a 3×3 beam sideband-separating Superconducting Spectroscopic Array Receiver (SSAR) system⁹¹ and using the position-switch on-the-fly mode, scanning the region at a rate of $50''$ per second. For details, refer Su et al.⁹². The *Planck*/353 GHz (resolution $\sim 5'$) polarization data, consisting of Stokes I, Q, and U maps, were extracted from the *Planck* Public Data Release 2⁹³ using the Multiple Frequency Cutout Visualization (PR2 Full Mission Map with PCCS2 Catalog; <https://irsa.ipac.caltech.edu/applications/planck/>). The pixel size and beam size were approximately $1'$ and $5'$, respectively. We processed the data and obtained the B-field map following the procedures outlined in Section 3.4 of Baug et al.⁹⁴ and the references therein.

Gravitational vector map

The local gravitational field in a star-forming region is a key factor influencing star formation and evolution. Mass distribution in a star-forming region determines the local gravitational field, which in turn affects the motion and dynamics of the gas and dust in the region. The gravitational field can cause the gas and dust to collapse, form dense cores, and eventually lead to the formation of stars. Understanding the local gravitational field in a star-forming region is important for studying star formation processes and the evolution of star-forming regions. The local gravitational field can be studied by observing the motion and distribution of gas and dust.

To determine the impact of gravity in the star-forming region, we estimated the projected gravitational vector field using the JCMT 850 μm dust continuum map. The direction and relative strength of local gravity at each point in a map can be determined by summing up the dust emission from surrounding pixels. This vector sum, calculated at each pixel, considers the directions and distances of every neighboring pixel, weighted by the dust emission. To use this

information to understand the local gravitational pull, it is assumed that the distribution of dust emission accurately reflects the distribution of total mass. This allows for the visualization of the direction of local gravity. The absolute strength of gravity can be scaled using a gas-to-dust mass ratio, but this ratio only impacts the magnitude and not the direction of local gravity vectors. The local projected gravitational force acting at a pixel position ($\vec{F}_{G,i}$) can be calculated using the polarization-intensity gradient technique^{95,96}. This method involves summing up the vectors of gravitational pulls from all neighboring pixel positions, which can be expressed as

$$\vec{F}_{G,i} = KI_i \sum_{j=1}^n \frac{I_j}{r_{ij}^2} \hat{r}$$

The equation for the local projected gravitational force at a pixel position ($\vec{F}_{G,i}$) considers the gravitational constant and the conversion from emission to total column density through the factor K . The intensities at pixel positions i and j (I_i and I_j) and the number of pixels within the relevant gravitational influence (n) are also included. The POS projected distance between pixel i and j ($r_{i,j}$) and the corresponding unity vector (\hat{r}) are used to determine the local gravitational vector field, which shows the direction and magnitude of the gravitational pull at each selected pixel. For this analysis, only the direction of the local gravitational forces is considered, and the distribution of dust is assumed to be a good approximation for the total mass distribution. The constant K is set to 1, and a lower threshold is introduced to exclude weak and symmetrical diffuse emission from the calculation. Diffuse emissions at distances outside the extension of our maps can be safely discarded. This is because any gravitational force will be completely canceled out by the emission's down-weighting caused by a rapidly decreasing $1/r^2$ factor and the tendency of the diffuse emission to become more azimuthally symmetrical at greater distances. This framework allows for interpreting and analyzing the local role of gravity and B-fields, their relative importance, spatial variations, systematic features, and statistical properties. In the analysis, we considered pixels within $4'$ diameter area with intensity higher than 16 mJy beam^{-1} (5σ), and those outside $4'$ diameter are masked. The resulting local gravitational vector field at each pixel in the dust emission map and at pixel positions where the B-field segment is present is shown in Extended Data Figure 5. It can be seen that the projected gravitational field vectors are directed toward the massive central hub, which indicates that the hub exerts a dominant effect on the overall gravitational field in the area.

Correlation between outflow and B-field

To investigate this further, an offset angle map is produced by taking the difference between the pixel-wise B-field angle and large-scale outflow position angle. The latter was obtained in the eastern region by averaging the angles of ejections from the chains of H_2 knots. These include the two eastern components of HH 169 with position angles (PAs) of approximately 80° and 65° , a bright compact H_2 bow at around 55° , and the current orientation of the jet at 45° . For the western part of the outflow, we used the PA of HH 168 at approximately 100° (please refer to Figure 6 of Cunningham et al.⁴²). A one-to-one correlation between the large-scale outflow and the B-field is seen in the East-West region (Extended Data Figure 7).

Estimation of Outflow ($E_{outflow}$), magnetic (E_B), gravitational (E_G) and kinetic (E_K) energy

We followed the procedure described in Section 3.2 of the Xu et al.⁹⁷ to calculate the outflow energy. From the average spectra of the ^{13}CO map, we observed that the channels with

velocities less than -15 km/s and greater than -5 km/s appear to be influenced by outflows. Therefore, we designated these two velocity ranges as the blue and red-shifted outflow lobes, respectively. For each channel within these ^{13}CO outflow lobes, we calculated the energy by considering both the channel mass and channel velocity. To improve accuracy, we subtracted the central velocity along each sightline to minimize the impact of large velocity gradients across the entire cloud. Using this approach, we determined the outflow energy to be 9.4 and 8.9×10^{38} erg for the blue and red-shifted lobes, respectively. We also calculated the magnetic energy (E_B) using the formula $E_B = \frac{B^2}{8\pi} V$, where B represents the mean B-field strength within a radius ‘ r ’, and $V = (4/3)\pi r^3$ is the corresponding volume. Additionally, we determined the gravitational energy (E_G) using the relation $E_G = (3/5) GM^2/r$, where M is the total mass within the radius ‘ r ’⁹⁸. The kinetic energy can be calculated using the relation $E_K = (3/2)M\sigma_v^2$, where σ_v is the velocity dispersion measured w.r.t the V_{LSR} ⁵⁹.

Significance of $\sin \omega$ map

The ideal magnetohydrodynamics (MHD) force equation can be written as⁵¹,

$$\rho \left(\frac{\partial}{\partial t} + v \cdot \nabla \right) v = -\nabla P - \rho \nabla \phi + \frac{B^2}{4\pi R} \sin \omega g + \frac{B^2}{4\pi R} \cos \omega n_g, \quad (1)$$

where $\nabla \phi$ represents the direction of local gravity and the term $\frac{B^2}{4\pi R} \sin \omega$ can be used to quantify the effectiveness of the B-field in opposing gravitational field. In particular, the factor $\sin \omega$ defines the fraction $\frac{B^2}{4\pi R}$ that can work against gravity to slow down or prohibit the gas motion driven by gravity. Larger offset angles (Figure 2(b)), as well as larger $\sin \omega$ values (Figure 2(c)) in the E-W region, suggest nearly orthogonal orientation between gravity and B-field. Since outflows have impacted the E-W region, we do not interpret $\sin \omega$ in terms of gravity versus B-field.

B-field strength using Davis-Chandrasekhar-Fermi (DCF) method

The DCF method has been used to estimate the B-field strengths in Cep A^{56,57}. This method assumes that the perturbations in the B-field are Alfvénic, which means the deviation in angle from the mean field direction is due to the distortion by small-scale non-thermal motions. Using this method, we can generate a map of the B-field strength by utilizing three quantities: polarization angle dispersion, gas number density, and non-thermal velocity dispersion. The moving box approximation method⁹⁹ has been adopted to produce the B-field angle dispersion map. Since the pixel and beam sizes of number density and velocity dispersion maps ($4''$, and $7.27''$, respectively) differ from those of the angle dispersion map ($12''$), we regridded these maps to a common bin size of $12''$, using the Kernel Application Package (KAPPA⁸³) task `wcsalign` and applied gaussian convolution to achieve a common beam size of $14''$. Then, we inserted the values of these three quantities and obtained the plane-of-sky B-field strength (B_{pos}) by the equation:

$$B_{\text{pos}}[\mu\text{G}] = Q \sqrt{4\pi\rho} \frac{\sigma_v}{\sigma_\theta} \approx 9.3 \sqrt{n(\text{H}_2)[\text{cm}^{-3}]} \frac{\Delta V[\text{km s}^{-1}]}{\sigma_\theta[\text{degree}]}, \quad (2)$$

Here, B_{pos} represents the B-field in the plane of the sky, $Q = 0.5$ is the correction factor recommended by Ostriker et al.¹⁰⁰, while $Q = 0.28$ is suggested by Liu et al.¹⁰¹ based on their simulation results for cases where the angular dispersion is less than 25° . In this context, ρ is

the gas density, σ_v is the nonthermal velocity dispersion, and σ_θ denotes the angular dispersion of the plane-of-sky component. In Equation 2¹⁰², $n(\text{H}_2)$ represents the number density ($n(\text{H}_2) = \rho/\mu m_{\text{H}}$) and ΔV_{NT} represents the FWHM nonthermal velocity dispersion ($\Delta V_{\text{NT}} = \sigma_v \sqrt{8 \ln 2}$). We assume a molecular weight $\mu = 2.8$ ¹⁰³, and this value is applied wherever required.

Measurement of B-field strength using Skalidis & Tassis method

Skalidis & Tassis⁵⁸ highlight the findings from observations indicating that turbulence in the interstellar medium (ISM) exhibits anisotropy and non-Alfvénic compressible modes, could have significant relevance. As a result, they put forward a new approach to estimate the B-field strength in the ISM that considers these compressible modes. This can be calculated as,

$$B_{ST} [\mu G] = \sqrt{2\pi\rho} \frac{\sigma_v}{\sqrt{\sigma_\theta}} \approx 1.742 \sqrt{n(\text{H}_2) [\text{cm}^{-3}]} \frac{\Delta V_{\text{NT}} [\text{kms}^{-1}]}{\sqrt{\sigma_\theta [\text{Degree}]}} \quad (3)$$

We propose a direct calculation of the B-field strength based on the B-field strength obtained using the DCF method, which can be represented as

$$B_{ST} = 0.186 \sqrt{\sigma_\theta [\text{Degree}]} B_{\text{DCF}} [\mu G] \quad (4)$$

If we have the B-field strength obtained through the DCF method and the angular dispersion (σ_θ), it is possible to directly calculate the B-field strength using the ST method. The B-field strength map obtained by both DCF and ST method are shown in Extended Data Figure 8.

Identification of infalling Gas structures using C¹⁸O spectral data

We aim to identify the infall velocity structures within the C¹⁸O emission that remain unaffected by outflows. We consider channels with velocities ranging from -12.5 to -8 km/s to achieve this. The other channels with velocities < -12.5 and > -8 km/s seem to be impacted by the bipolar outflows as they are associated with blue-shifted CO emission and a faint H₂ bow shock to the east, as well as with HH 168 to the west⁴². We ensure that the average spectra extracted over the 5' region of Cep A do not show asymmetric wings. Therefore, the channels we have used are not influenced by outflow activity. Since the emission is more concentrated towards the infall velocity structures, we compare the Dendrogram-identified structures to the CMU infall model. To achieve this objective, we adopt the methodology employed by Thieme et al.¹⁰⁴, which utilizes the `astrodendro` algorithm¹⁰⁵ to analyze data in position-position-velocity (PPV) space. The dendrogram algorithm initially selects the brightest pixels in the image cube to construct a tree structure. Subsequently, it progressively incorporates fainter pixels until a new local maximum is identified, creating a new structure. These structures are represented as the ‘leaves’ of the tree and are connected by ‘branches,’ which denote pixels that are not local maxima. Eventually, all structures merge to form a complete tree. Various parameters are provided as input to the algorithm, including a minimum noise threshold for the tree (σ_{min}), a minimum significance level for structures (δ_{min}), and the minimum number of pixels required for a structure to be considered independent ($n_{\text{pix,min}}$). We established the values of σ_{min} as 2σ , δ_{min} as σ , and $n_{\text{pix,min}}$ as 20 pixels. Determining these parameters involved an iterative process of testing different values to identify the configuration that revealed the most cohesive structures. Following this, the algorithm was applied to the C¹⁸O image cube,

identifying a structure highlighted in red within the dendrogram as shown in Extended Data Figure 3. This structure corresponds to an infalling envelope, aligning with the CMU-modeled infalling trajectories, as shown in Figure 6.

Column density map of the collapsing gas structure

We produced C¹⁸O column density under the assumption of local thermal equilibrium (LTE) by employing the procedures mentioned in Mangum & Shirley et al.¹⁰⁶. First, we created the integrated-intensity (moment 0) map of the extracted dendrogram structure, which is a gravitationally collapsing envelope. Then, using the integrated intensity emission $\int S_{\nu} \Delta\nu$ of each pixel, we made the column density by employing

$$N_{\text{C}^{18}\text{O}} = \frac{3c^2}{16\pi^3 \Omega_s S \mu^2 \nu^3} \left(\frac{Q_{\text{rot}}}{g_J g_K g_I} \right) \exp\left(\frac{E_u}{kT_{\text{ex}}} \right) \int S_{\nu} \Delta\nu.$$

More details on various parameters can be found at Thieme et al.¹⁰⁴. The obtained column density of the structure is transformed into the column density of molecular hydrogen (N(H₂)) utilizing the abundance ratios: [¹²C/¹³C] = 77, [¹⁶O/¹⁸O] = 560, and [H₂/¹²CO] = 1.1×10^{-4} ^{107,108}, resulting in [H₂/C¹⁸O] = 0.61×10^7 . Using the total H₂ column density, we then calculated the mass to be 120 M_⊙.

Herschel Column density map

We construct the column density (N(H₂)) and dust temperature (T_d) maps through spectral energy distribution (SED) fitting to all the data points of PACS 160 μm (11.4''), SPIRE 250 μm (18.1''), SPIRE 350 μm (24.9''), SPIRE 500 μm (36.4'') and JCMT 850 μm (4'') by keeping column density and temperature as free parameters. These are produced using the following relation¹⁰⁹,

$$S_{\nu}^{\text{beam}} = \left(\frac{N_{\text{H}_2}}{2.02 \times 10^{20} \text{ cm}^{-2}} \right) \times \left(\frac{\kappa_{\nu}}{0.01 \text{ cm}^2 \text{ g}^{-1}} \right) \times \left(\frac{\Theta_{\text{HPBW}}}{10 \text{ arcsec}} \right)^2 \\ \times \left(\frac{\lambda}{\text{mm}} \right)^{-3} \times \left(\exp \left(1.439 \left(\frac{\lambda}{\text{mm}} \right)^{-1} \left(\frac{T_d}{10 \text{ K}} \right)^{-1} \right) - 1 \right)^{-1}.$$

Eventually, we produced the 4'' N(H₂) map using the 4'' pixel size POL-2 850 μm continuum emission with the low resolution (36.4'') dust temperature map produced using the above equation. Here, we assume that within 36.4'' beam size, the 4'' size pixels with different intensities have the same dust temperature. For more details, refer to Eswaraiah et al.¹⁰⁸ and the references therein.

Cassen-Moosman-Ulrich (CMU) model

The CMU model describes the infalling particle trajectories around a central point mass in the gravitational collapse of a rotating, spherically symmetric cloud^{71-73,110}. Key assumptions include solid-body rotation of the cloud at a uniform angular velocity, treating the central star as a point mass, trajectory conservation of specific angular momentum, negligible pressure forces leading to ballistic trajectories, and exclusion of disc, envelope, and B-field.

The path of the infalling matter described by parabolic trajectory and the angular relations is given:

$$r = \frac{\sin^2 \theta_0}{1 - \frac{\cos \theta}{\cos \theta_0}} r_c,$$

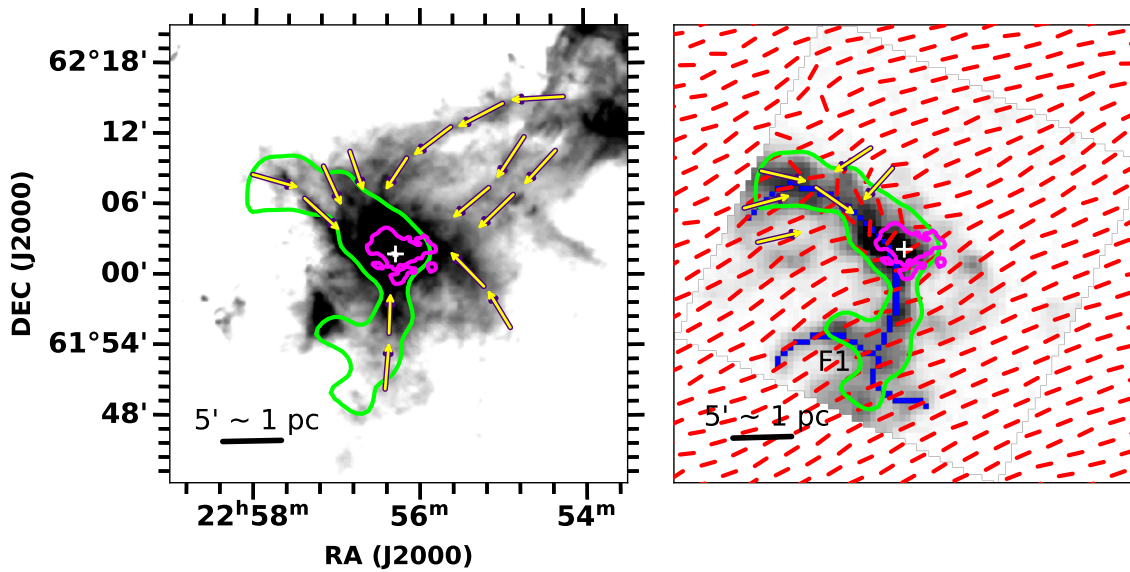
$$\cos \theta = \cos \nu \cos \theta_0, \text{ and}$$

$$\tan \nu = \tan(\phi - \phi_0) \sin \theta_0.$$

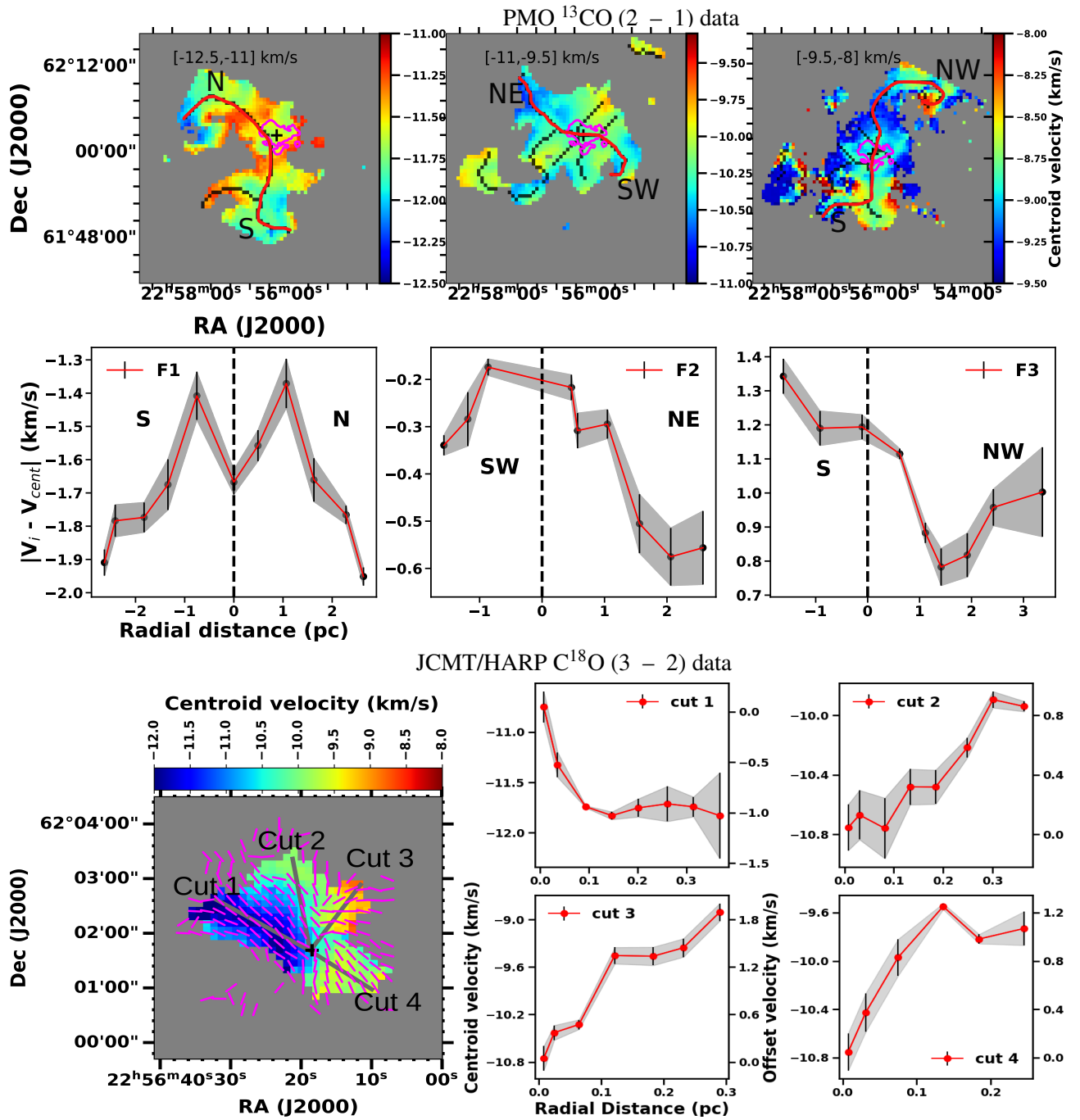
Here, θ_0 is the polar angle of the orbital plane for the particle trajectory, ϕ_0 is the azimuthal angle of the orbital apastron, and θ and ϕ are the polar and azimuthal angles of the particle after a time ' t .' r_c is the centrifugal radius, and ν denotes the angle of direction for the particle, measured from the origin to its farthest point from the star.

We modeled the trajectory with θ_0 varying from 1 to 180° and ϕ_0 from 0 to 360° with a protostellar mass of 15 M_\odot . To finalize the framework, we also incorporated the velocity of the particles. For more details, see Thieme et al.¹⁰⁴.

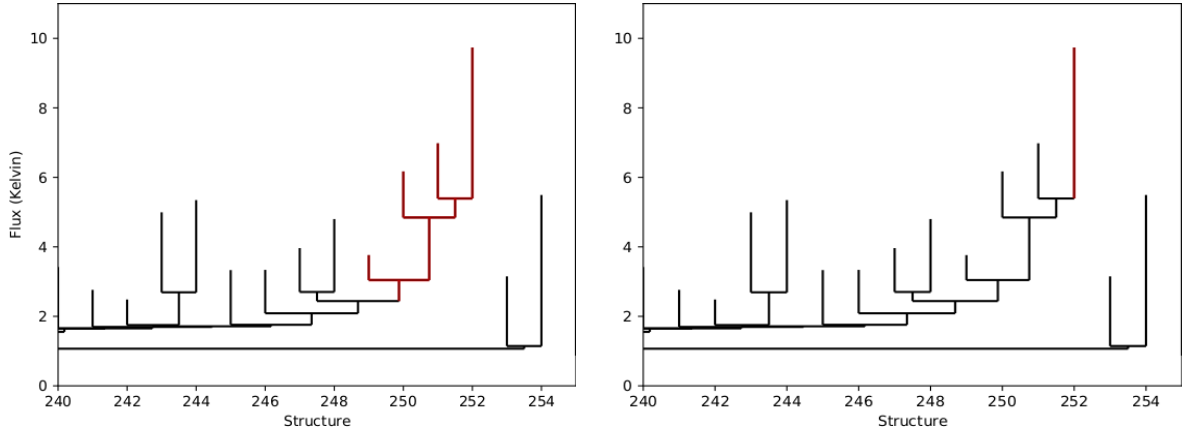
In the CMU model, trajectories trace the infalling matter uniformly from all directions, thereby depicting the scenario of global gravitational collapse. We have compared the observed dendrogram structure to the CMU-modeled trajectories in the PPV space by matching every model data point lying spatially within the half pixel-width ($\sim 7.27''$) of RA and Dec of the dendrogram data point and also lying within the half of spectral resolution (~ 0.17 km/s) of C¹⁸O cube. We determined the infall rate using the equation outlined in Pineda et al.¹¹¹.



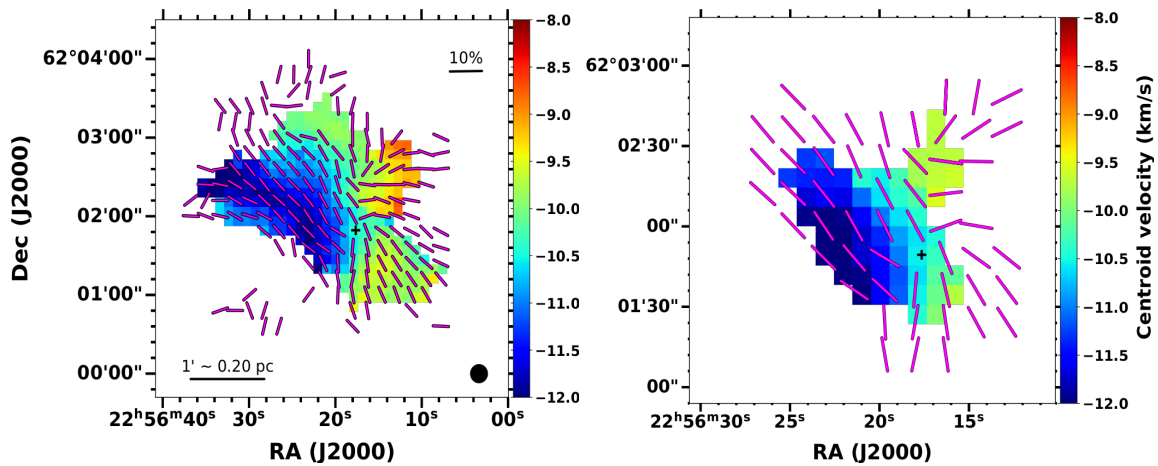
Extended Data Figure 1 | Left panel: The *Herschel*/SPIRE 250 μm dust continuum map revealing the large-scale extended filaments, as identified using yellow arrows, in Cep A cloud. Right panel: The cloud-scale B-field geometry (red segments) using the low-resolution (5') *Planck* 850 μm dust continuum polarization data. These B-fields are overlaid on the moment 0 map, revealing gas structure within the channels of $-12.5 - -11$ km/s. In both panels, a green contour, drawn at ^{13}CO integrated intensity of 3.5 K km/s, traces the identified ^{13}CO gas structure that is identified as F1 (see Extended Data Figure 2). The blue curve delineates the filament identified by the FILFINDER algorithm. Yellow vectors guide the bend in the B-field, possibly driven by the cloud's gravity. '+' sign represents the HW2 protostar. Magenta contour represents the POL-2 dust continuum emission (Stokes I) at 32 mJy/beam (equivalent to 10σ , where $\sigma = 3.2\text{mJy/beam}$).



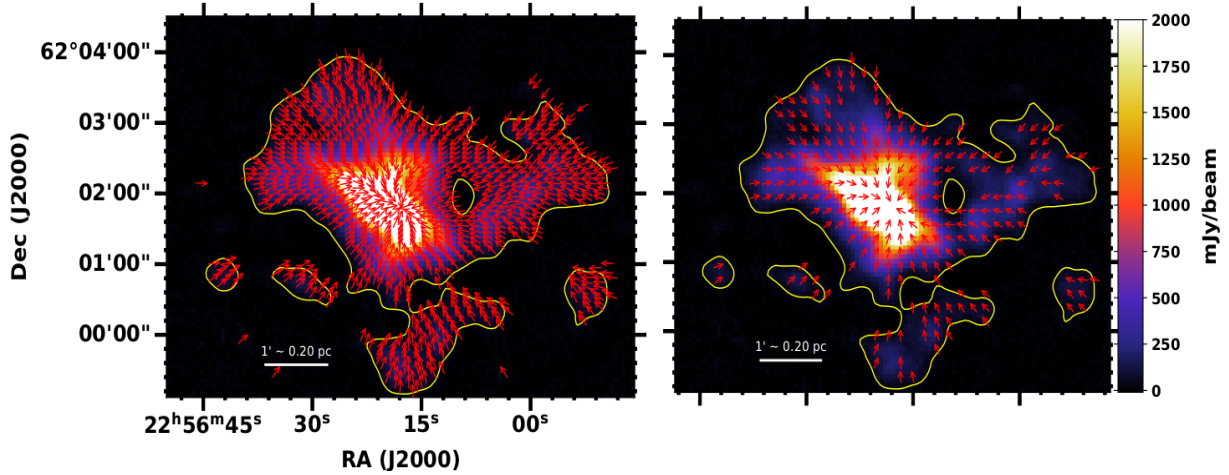
Extended Data Figure 2 | Gas structures and velocity gradients at the cloud and clump scales inferred based on the moment 1 maps using PMO ^{13}CO (top two rows) and JCMT/HARP C^{18}O (bottom panels) data. The magenta contour in the top panel corresponds to POL-2 dust continuum emission (Stokes I) at 32 mJy/beam (equivalent to 10σ , where $\sigma = 3.2$ mJy/beam is the rms noise in the dust continuum map). The ‘+’ sign represents the position of the HW2 protostar. The bottom panel displays four distinct cuts on the JCMT/HARP C^{18}O moment 1 map, while the bottom right panels present the corresponding velocity gradients extracted along these cuts. The dashed vertical line in the 2nd row and zero pc in the bottom right panels mark the position of the HW2 protostar.



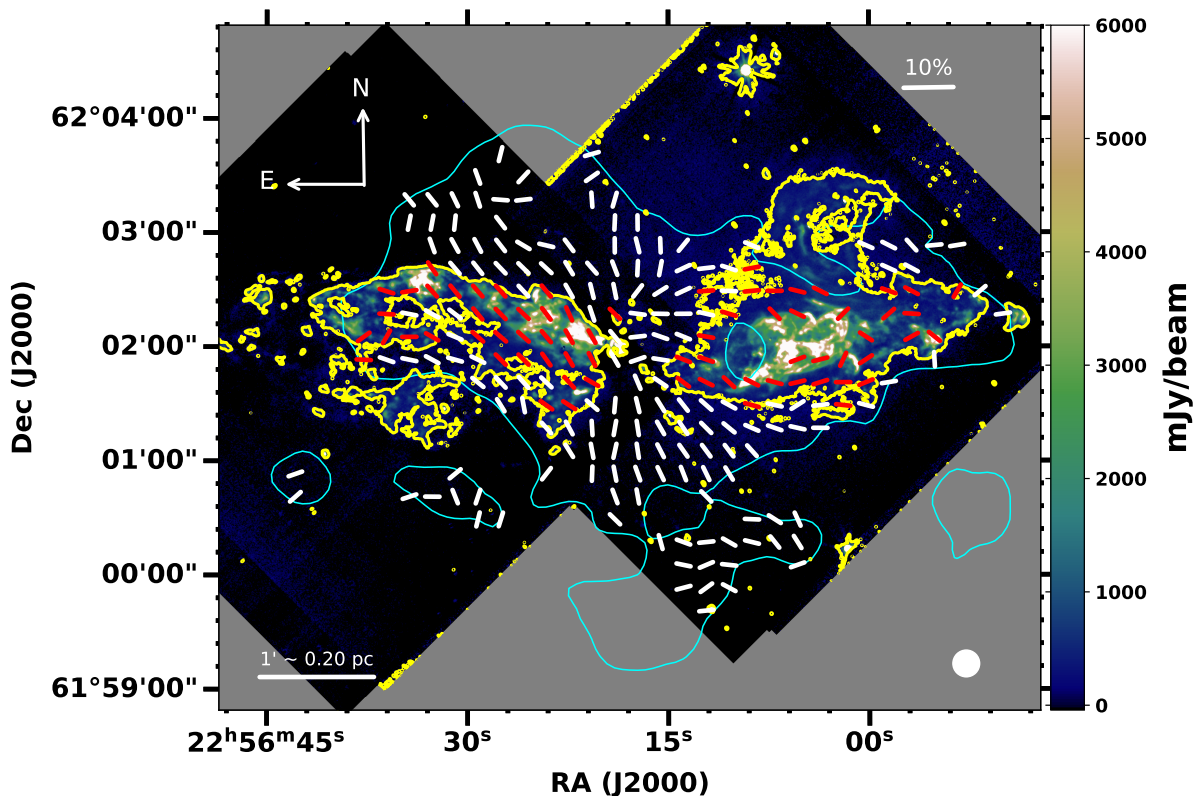
Extended Data Figure 3 | (Left): Dendrogram tree of $C^{18}O$ cube. Highlighted in red is the gravitationally collapsing envelope whose moment 1 map is shown in the left panel of Extended Data Figure 4. (Right): Same as a left panel but showing the more prominent leaf of the dendrogram tree, whose moment 1 map is shown in the right panel of Extended Data Figure 4



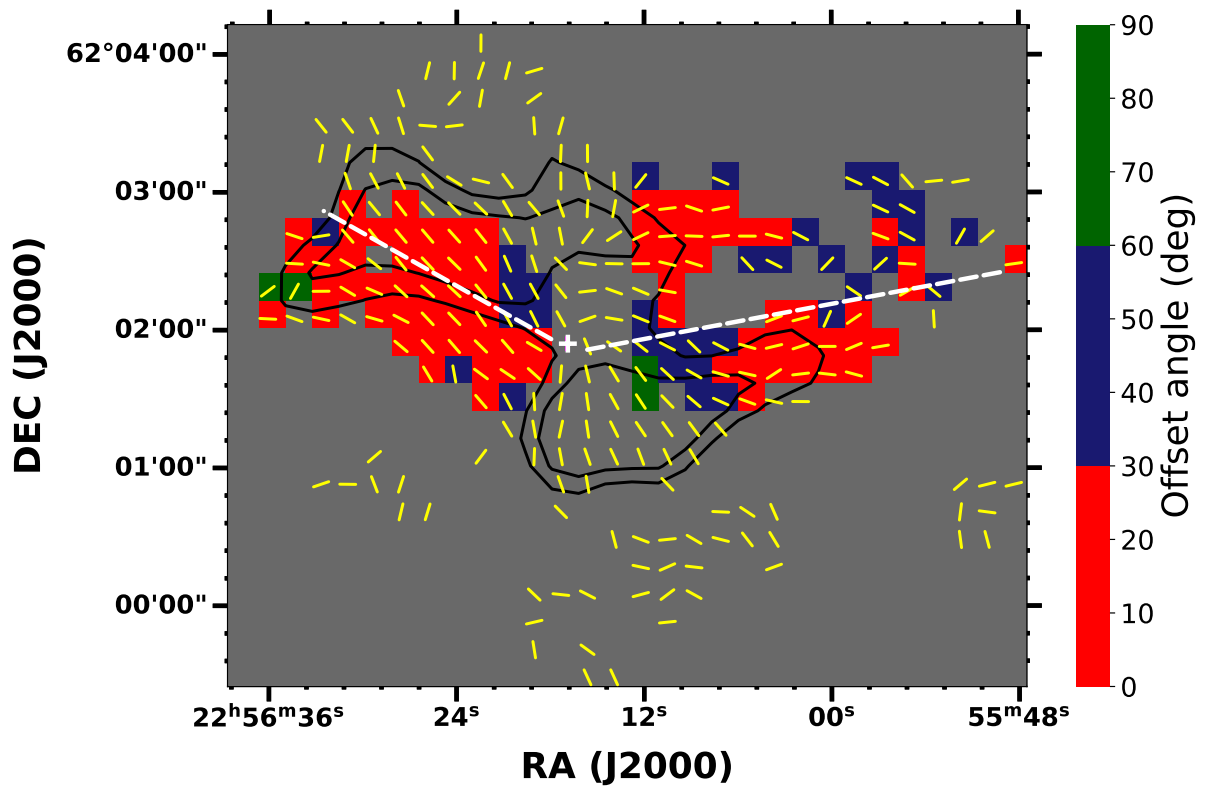
Extended Data Figure 4 | Moment 1 map of the identified gas structures based on the dendrogram analyses depicted in the left and right panel of Extended Data Figure 3. An infalling envelope comprises three gas structures that exhibit different velocities – visible in blue, cyan, and yellow/red, as shown in the left and right panels. Conspicuously, the B-field orientation associated with each gas structure is also different. The clump-scale infalling gas structure is extended close to the massive protostar Cep A HW2. The B-field got twisted at the location where these gas structures merge, as shown on the right panel.



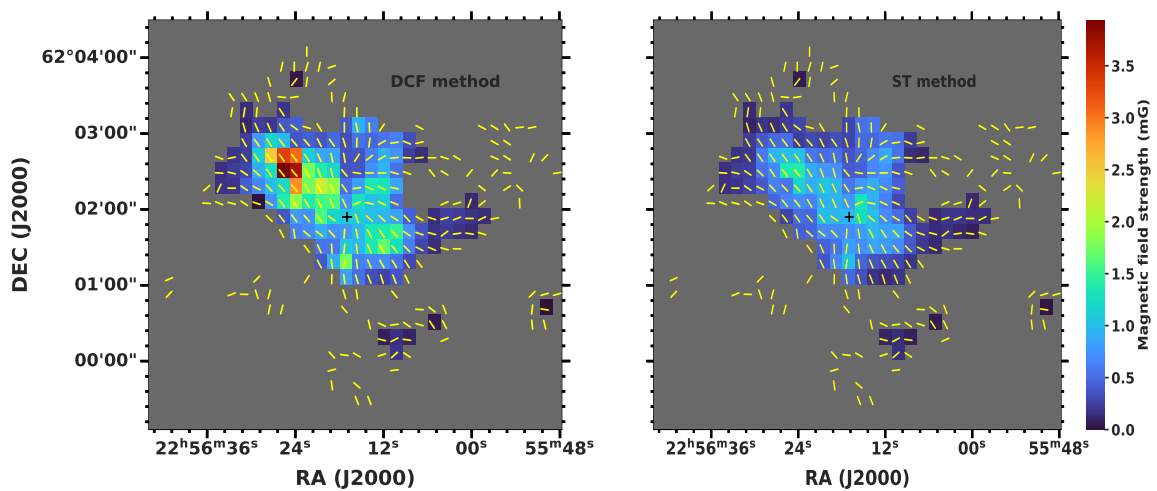
Extended Data Figure 5 | The gravitational field vector map of Cep A. (Left) Gravity vectors are shown on pixels with POL-2 Stokes I > 32 mJy/beam. (Right) Same as the left, but for only pixels having B-field measurements. The yellow contour in both panels corresponds to 10σ intensity of 32 mJy/beam, where $\sigma = 3.2$ mJy/beam is the rms noise of the Stokes I map.



Extended Data Figure 6 | The shock-excited H_2 emission at $2.12 \mu\text{m}$ (background map and yellow contours) tracing bipolar outflows emanated from the Cep A HW2⁴². Yellow contour is drawn at 200 mJy/beam. Red segments are distributed within the H_2 emission of 200 mJy/beam. The white segments lie in the regions with negligible H_2 emission of < 200 mJy/beam may trace the B-fields unperturbed by the outflows. Cyan contour is the same as the outer contour shown in Figure 1.



Extended Data Figure 7 | Offset map between the position angles of outflows and B-field. White dashed lines represent the mean position angles of the outflows.



Extended Data Figure 8 | B-field strength map using the DCF method (left) and the ST method (right). Yellow segments represent the POL-2 B-field. The '+' sign represents the position of the HW2 protostar. The colorbar applies to both the maps produced using the ST and DCF methods.

Author contribution

Chakali Eswaraiah (CE) has designed and initiated the project. CE and Sandhyarani Panigrahy (SP), in collaboration with Di Li, Shih-Ping Lai, Jia-Wei Wang, and Wen-Ping Chen, have acquired the JCMT SCUBA-2/POL-2 data. SP has led the data reduction and analyses of POL-2 data and other molecular lines data presented in the manuscript under the supervision of CE. SP and CE have come up with the first draft. Enrique Vázquez-Semadeni and Gilberto C. Gómez contributed their insights and streamlined the scientific discussions. Travis J. Thieme has contributed to the CMU modeling of the molecular lines data. Manash R. Samal and D. K. Ojha, as well as all other co-authors, have critically reviewed and contributed to improving the flow and contents of the manuscript.

Acknowledgements

CE acknowledges the financial support from grant RJF/2020/000071 as a part of the Ramanujan Fellowship awarded by the Science and Engineering Research Board (SERB), Department of Science and Technology (DST), Govt. of India. SP thanks the DST-INSPIRE Fellowship (No. IF200294) from the Department of Science and Technology (DST) for supporting the Ph.D. program. D.K.O. acknowledges the support of the Department of Atomic Energy, Government of India, under project identification No. RTI 4002. The East Asian Observatory operates the James Clerk Maxwell Telescope on behalf of The National Astronomical Observatory of Japan; Academia Sinica Institute of Astronomy and Astrophysics; the Korea Astronomy and Space Science Institute; the National Astronomical Research Institute of Thailand; Center for Astronomical Mega-Science (as well as the National Key R&D Program of China with No. 2017YFA0402700). Additional funding support is provided by the Science and Technology Facilities Council of the United Kingdom and participating universities and organizations in the United Kingdom and Canada. The Canada Foundation provided additional funds for the construction of SCUBA-2 for Innovation. The authors wish to recognize and acknowledge the significant cultural role and reverence that the summit of Maunakea has always had within the indigenous Hawaiian community. We are most fortunate to have the opportunity to conduct observations from this mountain. This research utilized data from the Milky Way Imaging Scroll Painting (MWISP) project, a multi-line ^{13}CO survey of the northern Galactic plane conducted with the PMO-13.7m telescope. We extend our gratitude to the MWISP working group, especially the staff at the PMO-13.7m telescope, for their ongoing support. The MWISP project is funded by China's National Key R&D Program (2017YFA0402701 grant) and the CAS Key Research Program of Frontier Sciences (QYZDJ-SSW-SLH047 grant). We thank Nathaniel Cunningham and John Bally for supplying the $2.12\ \mu\text{m}$ H_2 continuum-subtracted data and Henrik Beuther for providing the SMA polarimetry data. We thank Ian Stephens, M. S. Nanda Kumar, Jihye Hwang, Yuehui Ma, and Sheng-Jun Lin for the helpful discussions.

References

- [1] Kennicutt, Robert C. The role of massive stars in astrophysics. *Proceedings of the International Astronomical Union* **1**(S227), 3–11 (2005). Cambridge University Press.
- [2] Urquhart, J. S. *et al.* ATLASGAL—properties of compact H ii regions and their natal clumps. *Monthly Notices of the Royal Astronomical Society* **435**, 400–428 (2013).
- [3] Hennemann, M, Motte, F, Schneider, N, Didelon, P, Hill, T, Arzoumanian, D, Bontemps, Sylvain, Csengeri, T, André, Ph, Konyves, V, others. The spine of the swan: a Herschel study of the DR21 ridge and filaments in Cygnus X. *Astronomy & Astrophysics* **543**, L3 (2012). EDP Sciences.
- [4] Liu, Haiyu Baobab, Quintana-Lacaci, Guillermo, Wang, Ke, Ho, Paul TP, Li, Zhi-Yun, Zhang, Qizhou, Zhang, Zhi-Yu. The origin of OB clusters: from 10 pc to 0.1 pc. *The Astrophysical Journal* **745**, 1, 61 (2011). IOP Publishing.
- [5] Liu, Tie, Zhang, Qizhou, Kim, Kee-Tae, Wu, Yuefang, Lee, Chang-Won, Goldsmith, Paul F, Li, Di, Liu, Sheng-Yuan, Chen, Huei-Ru, Tatematsu, Ken'ichi, others. Discovery of an extremely wide-angle bipolar outflow in afgl 5142. *The Astrophysical Journal* **824**, 1, 31 (2016). IOP Publishing.
- [6] Peretto, Nicolas, Fuller, GA, Duarte-Cabral, Ana, Avison, A, Hennebelle, P, Pineda, JE, André, Ph, Bontemps, Sylvain, Motte, F, Schneider, N, others. Global collapse of molecular clouds as a formation mechanism for the most massive stars. *Astronomy & Astrophysics* **555**, A112 (2013). EDP Sciences.
- [7] Peretto, Nicolas, Fuller, GA, André, Ph, Arzoumanian, D, Rivilla, VM, Bardeau, S, Puer-tas, S Duarte, Fernandez, JP Guzman, Lenfestey, C, Li, G-X, others. SDC13 infrared dark clouds: Longitudinally collapsing filaments?. *Astronomy & Astrophysics* **561**, A83 (2014). EDP Sciences.
- [8] Yuan, Jinghua, Li, Jin-Zeng, Wu, Yuefang, Ellingsen, Simon P, Henkel, Christian, Wang, Ke, Liu, Tie, Liu, Hong-Li, Zavagno, Annie, Ren, Zhiyuan, others. High-mass star formation through filamentary collapse and clump-fed accretion in G22. *The Astrophysical Journal* **852**, 1, 12 (2017). IOP Publishing.
- [9] Zhou, Jian-Wen, Liu, Tie, Evans, Neal J, Garay, Guido, Goldsmith, Paul F, Gómez, Gilberto C, Vázquez-Semadeni, Enrique, Liu, Hong-Li, Stutz, Amelia M, Wang, Ke, others. ATOMS: ALMA Three-millimeter Observations of Massive Star-forming regions—XI. From inflow to infall in hub-filament systems. *Monthly Notices of the Royal Astronomical Society* **514**, 4, 6038–6052 (2022). Oxford University Press.
- [10] Vázquez-Semadeni, Enrique, Palau, Aina, Ballesteros-Paredes, Javier, Gómez, Gilberto C., Zamora-Avilés, Manuel (2019). Global hierarchical collapse in molecular clouds. Towards a comprehensive scenario. *Monthly Notices of the Royal Astronomical Society*, **490**(3), 3061–3097. Oxford University Press. 10.1093/mnras/stz2736. arXiv, 1903.11247, astro-ph.GA. <https://ui.adsabs.harvard.edu/abs/2019MNRAS.490.3061V>, Provided by the SAO/NASA Astrophysics Data System.

- [11] Vázquez-Semadeni, E., Gómez, G. C., González-Samaniego, A. (2024). Multiscale accretion in dense cloud cores and the delayed formation of massive stars. *Monthly Notices of the Royal Astronomical Society*, **530**(3), 3445–3457. Oxford University Press.
- [12] Zhang, Q., Wang, Y., Pillai, T., Rathborne, J. (2009). Fragmentation at the earliest phase of massive star formation. *The Astrophysical Journal*, **696**(1), 268. IOP Publishing.
- [13] Klessen, Ralf S, Heitsch, Fabian, Mac Low, Mordecai-Mark. Gravitational collapse in turbulent molecular clouds. I. Gasdynamical turbulence. *The Astrophysical Journal* **535**, 2, 887 (2000). IOP Publishing.
- [14] Federrath, Christoph. Inefficient star formation through turbulence, magnetic fields and feedback. *Monthly Notices of the Royal Astronomical Society* **450**, 4, 4035–4042 (2015). Oxford University Press.
- [15] Tang, Ya-Wen, Koch, Patrick M, Peretto, Nicolas, Novak, Giles, Duarte-Cabral, Ana, Chapman, Nicholas L, Hsieh, Pei-Ying, Yen, Hsi-Wei. Gravity, magnetic field, and turbulence: relative importance and impact on fragmentation in the infrared dark cloud G34.43+00.24. *The Astrophysical Journal* **878**, 1, 10 (2019). IOP Publishing.
- [16] Pattle, Kate, Fissel, Laura, Tahani, Mehrnoosh, Liu, Tie, Ntormousi, Evangelia. Magnetic fields in star formation: from clouds to cores. *arXiv preprint arXiv:2203.11179* (2022).
- [17] Treviño-Morales, SP, Fuente, A, Sánchez-Monge, Á, Kainulainen, J, Didelon, P, Suri, S, Schneider, N, Ballesteros-Paredes, J, Lee, Y-N, Hennebelle, P, others. Dynamics of cluster-forming hub-filament systems-The case of the high-mass star-forming complex Monoceros R2. *Astronomy & Astrophysics* **629**, A81 (2019). EDP Sciences.
- [18] Kumar, MSN, Arzoumanian, D, Men’Shchikov, A, Palmeirim, P, Matsumura, M, Inutsuka, Si. Filament coalescence and hub structure in Mon R2-Implications for massive star and cluster formation. *Astronomy & Astrophysics* **658**, A114 (2022). EDP Sciences.
- [19] Wang, J.-W., Lai, S.-P., Eswaraiah, C., Pattle, K., Di Francesco, J., Johnstone, D., Koch, P. M., Liu, T., Tamura, M., Furuya, R. S., others (2019). JCMT BISTRO Survey: Magnetic Fields within the Hub-filament Structure in IC 5146. *The Astrophysical Journal*, **876**(1), 42. IOP Publishing.
- [20] Wang, J.-W., Koch, P. M., Galván-Madrid, R., Lai, S.-P., Liu, H. B., Lin, S.-J., Pattle, K. (2020). Formation of the Hub–Filament System G33.92+0.11: Local Interplay between Gravity, Velocity, and Magnetic Field. *The Astrophysical Journal*, **905**(2), 158. IOP Publishing.
- [21] Beuther, H., Soler, J. D., Linz, H., Henning, T., Gieser, C., Kuiper, R., Vlemmings, W., Hennebelle, P., Feng, S., Smith, R., et al. (2020). Gravity and rotation drag the magnetic field in high-mass star formation. *The Astrophysical Journal*, **904**(2), 168. IOP Publishing.
- [22] Wang, J.-W., Koch, P. M., Clarke, S. D., Fuller, G., Peretto, N., Tang, Y.-W., Yen, H.-W., Lai, S.-P., Ohashi, N., Arzoumanian, D., et al. (2024). Filamentary network and magnetic field structures revealed with BISTRO in the high-mass star-forming region NGC 2264: Global properties and local magnetogravitational configurations. *The Astrophysical Journal*, **962**(2), 136. IOP Publishing.

- [23] Collaboration, Planck, Aghanim, N, Akrami, Y, Alves, MIR, Ashdown, M, Aumont, J, Baccigalupi, C, Ballardini, M, Banday, AJ, Barreiro, RB, others. Planck 2018 results. *A&a* **641**, A12 (2020).
- [24] Soler, JD, Ade, PAR, Angilè, FE, Ashton, P, Benton, SJ, Devlin, MJ, Dober, B, Fissel, LM, Fukui, Y, Galitzki, N, others. The relation between the column density structures and the magnetic field orientation in the Vela C molecular complex. *Astronomy & Astrophysics* **603**, A64 (2017). EDP Sciences.
- [25] Soler, Juan D. Using Herschel and Planck observations to delineate the role of magnetic fields in molecular cloud structure. *Astronomy & Astrophysics* **629**, A96 (2019). EDP Sciences.
- [26] Soler, Juan D, Hennebelle, Patrick. What are we learning from the relative orientation between density structures and the magnetic field in molecular clouds?. *Astronomy & Astrophysics* **607**, A2 (2017). EDP Sciences.
- [27] Gómez, Gilberto C, Vázquez-Semadeni, Enrique, Zamora-Avilés, Manuel (2018). The magnetic field structure in molecular cloud filaments. *Monthly Notices of the Royal Astronomical Society*, **480**, 3, 2939–2944. Oxford University Press.
- [28] Pillai, Thushara GS, Clemens, Dan P, Reissl, Stefan, Myers, Philip C, Kauffmann, Jens, Lopez-Rodriguez, Enrique, Alves, Felipe O, Franco, GAP, Henshaw, Jonathan, Menten, Karl M, others. Magnetized filamentary gas flows feeding the young embedded cluster in Serpens South. *Nature Astronomy* **4**, 12, 1195–1201 (2020). Nature Publishing Group UK London.
- [29] Arzoumanian, Doris, Furuya, Ray S, Hasegawa, Tetsuo, Tahani, M, Sadavoy, S, Hull, Charles LH, Johnstone, D, Koch, Patrick M, Inutsuka, S-i, Doi, Yasuo, others. Dust polarized emission observations of NGC 6334-BISTRO reveals the details of the complex but organized magnetic field structure of the high-mass star-forming hub-filament network. *Astronomy & Astrophysics* **647**, A78 (2021). EDP Sciences.
- [30] Kwon, Woojin, Pattle, Kate, Sadavoy, Sarah, Hull, Charles LH, Johnstone, Doug, Ward-Thompson, Derek, Di Francesco, James, Koch, Patrick M, Furuya, Ray, Doi, Yasuo, others. B-fields in Star-forming Region Observations (BISTRO): Magnetic fields in the filamentary structures of Serpens Main. *The Astrophysical Journal* **926**, 2, 163 (2022). IOP Publishing.
- [31] Liu, Hong-Li, Tej, Anandmayee, Liu, Tie, Goldsmith, Paul F., Stutz, Amelia, Juvela, Mika, Qin, Sheng-Li, Xu, Feng-Wei, Bronfman, Leonardo, Evans, Neal J., Saha, Anindya, Issac, Namitha, Tatematsu, Ken'ichi, Wang, Ke, Li, Shanghuo, Zhang, Siju, Baug, Tapas, Dewangan, Lokesh, Wu, Yue-Fang, Zhang, Yong, Lee, Chang Won, Liu, Xun-Chuan, Zhou, Jianwen, Soam, Archana (2022). ATOMS: ALMA Three-millimeter Observations of Massive Star-forming Regions - IX. A Pilot Study Towards IRDC G034.43+00.24 on Multi-scale Structures and Gas Kinematics. *Monthly Notices of the Royal Astronomical Society*, **511**(3), 4480–4489. Oxford University Press. 10.1093/mnras/stac378. 2202.11307.
- [32] Sanhueza, P., Girart, J. M., Padovani, M., Galli, D., Hull, C. L. H., Zhang, Q., Cortes, P., Stephens, I. W., Fernández-López, M., Jackson, J. M., et al. (2021). Gravity-driven

- magnetic field at 1000 au scales in high-mass star formation. *The Astrophysical Journal Letters*, **915**(1), L10. IOP Publishing.
- [33] Cortes, P. C., Girart, J. M., Sanhueza, P., Liu, J., Martin, S., Stephens, I. W., Beuther, H., Koch, P. M., Fernandez-Lopez, M., Sanchez-Monge, A., et al. (2024). MagMar III—Resisting the Pressure: Is the Magnetic Field Overwhelmed in NGC 6334I?. arXiv preprint arXiv:2406.14663.
- [34] Curran, R. L., Chrysostomou, A. (2007). Magnetic fields in massive star-forming regions. *Monthly Notices of the Royal Astronomical Society*, **382**(2), 699–716. Oxford University Press. 10.1111/j.1365-2966.2007.12399.x. <https://doi.org/10.1111/j.1365-2966.2007.12399.x>. <https://academic.oup.com/mnras/article-pdf/382/2/699/3426399/mnras0382-0699.pdf>.
- [35] Lai, Shih-Ping (2001). Interferometric mapping of magnetic fields in star-forming regions. University of Illinois, Urbana-Champaign. October. *Physics: Astronomy and Astrophysics*. <https://ui.adsabs.harvard.edu/abs/2001PhDT.....1L>. Provided by the SAO/NASA Astrophysics Data System.
- [36] Beuther, H., Gieser, C., Soler, J. D., Zhang, Q., Rao, R., Semenov, D., Henning, Th., Pudritz, R., Peters, T., Klaassen, P., others Density distributions, magnetic field structures and fragmentation in high-mass star formation. *arXiv preprint arXiv:2311.11874* (2023).
- [37] Vlemmings, W. H. T., Diamond, P. J., van Langevelde, H. J., Torrelles, J. M. (2006). The magnetic field in the star-forming region Cepheus A from H₂O maser polarization observations. *Astronomy & Astrophysics*, **448**(2), 597–611. EDP Sciences. 10.1051/0004-6361:20054275. arXiv, astro-ph/0510452, astro-ph. <https://ui.adsabs.harvard.edu/abs/2006A&A...448..597V>, Provided by the SAO/NASA Astrophysics Data System.
- [38] Li, Hua-bai (2017). *The Tai Chi in Star Formation*. Morgan & Claypool Publishers. 2053-2571. 978-1-6817-4293-9. 10.1088/978-1-6817-4293-9. <https://dx.doi.org/10.1088/978-1-6817-4293-9>.
- [39] Dzib, Sergio, Loinard, Laurent, Rodríguez, Luis F, Mioduszewski, Amy J, and Torres, Rosa M. VLBA Determination of the distance to nearby star-forming regions. VI. The distance to the young stellar object HW 9 in Cepheus A. *The Astrophysical Journal* **733**, 1, 71 (2011). IOP Publishing.
- [40] Yu, Zhi-Yao, Nagahama, Tomoo, & Fukui, Yasuo. (1996). The New Observation of C18O (J= 1–0) Molecular Emission in the Cepheus OB3 Molecular Cloud. *The Astrophysical Journal*, **471**(2), 867. IOP Publishing.
- [41] Koppelaar, K., Sargent, A.I., Nordh, L., Van Duinen, R.J., Aalders, J.W.G. Observations of new far infrared sources in the Cepheus OB 3 molecular cloud. *Astronomy and Astrophysics*, **75**(1-2), L1–L3 (1979).
- [42] Cunningham, N. J., Moeckel, N., Bally, J. (2009). A Pulsed, Precessing Jet in Cepheus A. *The Astrophysical Journal*, **692**(2), 943. IOP Publishing.
- [43] Sanna, A., Moscadelli, L., Surcis, G., Van Langevelde, H. J., Torstensson, K. J. E., & Sobolev, A. M. (2017). Planar infall of CH₃OH gas around Cepheus A HW2. *Astronomy & Astrophysics*, **603**, A94. EDP Sciences.

- [44] Pattle, Kate, Ward-Thompson, Derek, Berry, David, Hatchell, Jennifer, Chen, Huei-Ru, Pon, Andy, Koch, Patrick M., Kwon, Woojin, Kim, Jongsoo, Bastien, Pierre, et al. (2017). The JCMT BISTRO survey: the magnetic field strength in the Orion A filament. *The Astrophysical Journal*, **846**(2), 122. IOP Publishing.
- [45] Greaves, J. S. & Holland, W. S. & Jenness, T. & Chrysostomou, A. & Berry, D. S. & Murray, A. G. & Tamura, M. & Robson, E. I. & Ade, P. A. R. & Nartallo, R. & others (2003). A submillimetre imaging polarimeter at the James Clerk Maxwell Telescope. *Monthly Notices of the Royal Astronomical Society*, **340**(2), 353–361. The Royal Astronomical Society.
- [46] Matthews, B. C., McPhee, C. A., Fissel, L. M., & Curran, R. L. (2009). The Legacy of SCUPOL: 850 μm Imaging Polarimetry from 1997 to 2005. *The Astrophysical Journal Supplement Series*, **182**(1), 143. IOP Publishing.
- [47] Curran, R. L. & Chrysostomou, A. (2007). Magnetic fields in massive star-forming regions. *Monthly Notices of the Royal Astronomical Society*, **382**(2), 699–716. Blackwell Publishing Ltd Oxford, UK.
- [48] Pudritz, R. E., Ray, T. P. (2019). The role of magnetic fields in protostellar outflows and star formation. *Frontiers in Astronomy and Space Sciences*, **6**, 54. Frontiers Media SA.
- [49] Mignon-Risse, R., González, M., Commerçon, B. (2023). The role of magnetic fields in the formation of multiple massive stars. *Astronomy & Astrophysics*, **673**, A134. EDP Sciences.
- [50] Oliva, A., Kuiper, R. (2023). Modeling disks and magnetic outflows around a forming massive star—I. Investigating the two-layer structure of the accretion disk. *Astronomy & Astrophysics*, **669**, A80. EDP Sciences.
- [51] Koch, Patrick M, Tang, Ya-Wen, Ho, Paul TP, Yen, Hsi-Wei, Su, Yu-Nung, Takakuwa, Shigehisa. Polarization properties and magnetic field structures in the high-mass star-forming region W51 observed with ALMA. *The Astrophysical Journal* **855**, 39 (2018), IOP Publishing.
- [52] Koch, Patrick M., Tang, Ya-Wen, Ho, Paul T. P. Magnetic field strength maps for molecular clouds: a new method based on a polarization–intensity gradient relation. *The Astrophysical Journal* **747**(1), 79 (2012). IOP Publishing.
- [53] Caselli, P., Walmsley, C. M., Terzieva, R., & Herbst, E. (1998). The ionization fraction in dense cloud cores. *The Astrophysical Journal*, **499**(1), 234. IOP Publishing.
- [54] Blackman, E. G. (2013). On deriving flux freezing in magnetohydrodynamics by direct differentiation. *European Journal of Physics*, **34**(2), 489. IOP Publishing.
- [55] Das, H. K. & Gronke, M. (2024). Magnetic fields in multiphase turbulence: impact on dynamics and structure. *Monthly Notices of the Royal Astronomical Society*, **527**(1), 991–1013. Oxford University Press.
- [56] Davis Jr, L. (1951). The strength of interstellar magnetic fields. *Physical Review*, **81**(5), 890. APS.

- [57] Chandrasekhar, S., Fermi, E. (1953). Problems of gravitational stability in the presence of a magnetic field. *Astrophysical Journal*, 116–141. American Astronomical Society.
- [58] Skalidis, R., Tassis, K. (2021). High-accuracy estimation of magnetic field strength in the interstellar medium from dust polarization. *Astronomy & Astrophysics*, **647**, A186. EDP Sciences.
- [59] Camacho, V., Vázquez-Semadeni, E., Palau, A., Zamora-Avilés, M. (2023). The kinetic and magnetic energy budget of hub-filament systems during the gravitational fragmentation of molecular clouds. *Monthly Notices of the Royal Astronomical Society*, **523**(3), 3376–3392. Oxford University Press.
- [60] Heitsch, Fabian, Hartmann, Lee W., Burkert, Andreas. Fragmentation of shocked flows: gravity, turbulence, and cooling. *The Astrophysical Journal* **683**, 2, 786 (2008). IOP Publishing.
- [61] Heitsch, Fabian, Stone, James M., Hartmann, Lee W.. Effects of magnetic field strength and orientation on molecular cloud formation. *The Astrophysical Journal* **695**, 1, 248 (2009). IOP Publishing.
- [62] Inoue, Tsuyoshi, Inutsuka, Shu-ichiro. Two-fluid magnetohydrodynamic simulations of converging HI flows in the interstellar medium. I. Methodology and basic results. *The Astrophysical Journal* **687**, 1, 303 (2008). IOP Publishing.
- [63] Inoue, Tsuyoshi, Inutsuka, Shu-ichiro. Two-fluid magnetohydrodynamics simulations of converging H i flows in the interstellar medium. II. Are molecular clouds generated directly from a warm neutral medium?. *The Astrophysical Journal* **704**, 1, 161 (2009). IOP Publishing.
- [64] Inoue, Tsuyoshi, Inutsuka, Shu-ichiro. Formation of turbulent and magnetized molecular clouds via accretion flows of H i clouds. *The Astrophysical Journal* **759**, 1, 35 (2012). IOP Publishing.
- [65] Vázquez-Semadeni, Enrique, Banerjee, Robi, Gómez, Gilberto C., Hennebelle, Patrick, Duffin, Dennis, Klessen, Ralf S.. Molecular cloud evolution–IV. Magnetic fields, ambipolar diffusion and the star formation efficiency. *Monthly Notices of the Royal Astronomical Society* **414**, 3, 2511–2527 (2011). Blackwell Publishing Ltd Oxford, UK.
- [66] Heitsch, Fabian, Hartmann, Lee. Accretion and diffusion time-scales in sheets and filaments. *Monthly Notices of the Royal Astronomical Society* **443**, 1, 230–240 (2014). Oxford University Press.
- [67] Lazarian, A. Reconnection diffusion in turbulent fluids and its implications for star formation. *Space Science Reviews* **181**, 1–59 (2014). Springer.
- [68] Körtgen, Bastian, Banerjee, Robi. Impact of magnetic fields on molecular cloud formation and evolution. *Monthly Notices of the Royal Astronomical Society* **451**, 3, 3340–3353 (2015). Oxford University Press.
- [69] Zamora-Avilés, Manuel, Vázquez-Semadeni, Enrique, Körtgen, Bastian, Banerjee, Robi, Hartmann, Lee (2018). Magnetic suppression of turbulence and the star formation activity of molecular clouds. *Monthly Notices of the Royal Astronomical Society*, **474**(4), 4824–4836. Oxford University Press.

- [70] Vlemmings, WHT, Surcis, G, Torstensson, KJE, van Langevelde, HJ (2010). *Magnetic field regulated infall on the disc around the massive protostar Cepheus A HW2*. *Monthly Notices of the Royal Astronomical Society*, **404**(1), 134–143. Blackwell Publishing Ltd Oxford, UK.
- [71] Ulrich, R. K. (1976). An infall model for the T Tauri phenomenon. *Astrophysical Journal*, **210**, 377–391.
- [72] Cassen, P., Moosman, A. (1981). On the formation of protostellar disks. *Icarus*, **48**(3), 353–376. Elsevier.
- [73] Chevalier, R. A. (1983). The environments of T Tauri stars. *Astrophysical Journal, Part 1* (ISSN 0004-637X), **268**, 753–765. Research supported by the University of Virginia.
- [74] Beuther, H., Schilke, P., Sridharan, T. K., Menten, K. M., Walmsley, C. M., Wyrowski, F. Massive molecular outflows. *Astronomy & Astrophysics* **383**, 892–904 (2002). EDP Sciences.
- [75] Zhang, Q., Hunter, T. R., Brand, J., Sridharan, T. K., Cesaroni, R., Molinari, S., Wang, J., Kramer, M. (2005). Search for CO Outflows toward a Sample of 69 High-Mass Protostellar Candidates. II. Outflow Properties. *The Astrophysical Journal*, **625**(2), 864. 10.1086/429660, <https://dx.doi.org/10.1086/429660>.
- [76] Grave, JMC & Kumar, MSN. Spitzer-IRAC GLIMPSE of high mass protostellar objects-II. SED modelling of a bona fide sample. *Astronomy & Astrophysics* **498**, 1, 147–159 (2009), EDP Sciences.
- [77] Hosokawa, Takashi and Omukai, Kazuyuki. Evolution of massive protostars with high accretion rates. *The Astrophysical Journal* **691**, 823 (2009).
- [78] Curiel, Salvador, Trinidad, Miguel A, Cantó, Jorge, Rodríguez, Luis F, Torrelles, José M, Ho, Paul TP, Patel, Nimesh A, Greenhill, Lincoln, Gómez, José F, Garay, Guido, others (2001). Detection of a candidate for the exciting source of the expanding water maser bubble in Cepheus A. *The Astrophysical Journal*, **564**, 1, L35. IOP Publishing.
- [79] Curiel, Salvador, Ho, PTP, Patel, NA, Torrelles, JM, Rodríguez, LF, Trinidad, MA, Cantó, J, Hernández, L, Gómez, JF, Garay, G, others (2006). Large proper motions in the jet of the high-mass YSO Cepheus A HW2. *The Astrophysical Journal*, **638**, 2, 878. IOP Publishing.
- [80] Friberg, P., Bastien, P., Berry, D., Savini, G., Graves, S. F., Pattle, K. (2016). POL-2: a polarimeter for the James-Clerk-Maxwell telescope. Millimeter, Submillimeter, and Far-Infrared Detectors and Instrumentation for Astronomy VIII, **9914**, 991403. SPIE.
- [81] Dempsey, J. T., Friberg, P., Jenness, T., et al. (2013). *MNRAS*, **430**, 2534.
- [82] Jenness, T., Currie, M. J., Tilanus, R. P. J., Cavanagh, B., Berry, D. S., Leech, J., Rizzi, L. (2015). Automated reduction of sub-millimetre single-dish heterodyne data from the James Clerk Maxwell Telescope using ORAC-DR. *Monthly Notices of the Royal Astronomical Society*, **453**(1), 73–88. Oxford University Press.

- [83] Currie, M. J., Draper, P. W., Berry, D. S., Jenness, T., Cavanagh, B., Economou, F. (2008). Starlink Software Developments. *Astronomical Data Analysis Software and Systems XVII*, **394**, 650. ASP.
- [84] Crutcher, Richard M. (2012). Magnetic fields in molecular clouds. *Annual Review of Astronomy and Astrophysics*, **50**(1), 29–63. Annual Reviews.
- [85] Li, Hua-Bai (2021). Magnetic fields in molecular clouds—observation and interpretation. *Galaxies*, **9**(2), 41. MDPI.
- [86] Fernández-López, Manuel, Stephens, IW, Girart, JM, Looney, L, Curiel, S, Segura-Cox, D, Eswaraiah, C, Lai, S-P. 1.3 mm polarized emission in the circumstellar disk of a massive protostar. *The Astrophysical Journal* **832**, 2, 200 (2016), IOP Publishing.
- [87] Comito, C., Schilke, P., Endesfelder, U., Jiménez-Serra, I., Martín-Pintado, J. (2007). High-resolution study of a star-forming cluster in the Cepheus A HW2 region. *Astronomy & Astrophysics*, **469**(1), 207–211. EDP Sciences.
- [88] Bottinelli, S. and Williams, J. P. Modeling the millimeter emission from the Cepheus A young stellar cluster: Evidence for large scale collapse. *Astron. Astrophys.* **421**, 1113–1119 (2004). <https://doi.org/10.1051/0004-6361:20035640>.
- [89] Kwon, W., Stephens, I. W., Tobin, J. J., Looney, L. W., Li, Z.-Y., Van Der Tak, F. F. S., Crutcher, R. M. Highly ordered and pinched magnetic fields in the class 0 protobinary system L1448 IRS 2. *The Astrophysical Journal* **879**(1), 25 (2019). IOP Publishing.
- [90] Buckle, J. V., Hills, R. E., Smith, H., Dent, W. R. F., Bell, G., Curtis, E. I., Dace, R., Gibson, H., Graves, S. F., Leech, J., et al. (2009). HARP/ACIS: a submillimetre spectral imaging system on the James Clerk Maxwell Telescope. *Monthly Notices of the Royal Astronomical Society*, **399**(2), 1026–1043. Blackwell Publishing Ltd, Oxford, UK.
- [91] Shan, W., Yang, J., Shi, S., Yao, Q., Zuo, Y., Lin, Z., Chen, S., Zhang, X., Duan, W., Cao, A., et al. (2012). Development of superconducting spectroscopic array receiver: A multibeam 2SB SIS receiver for millimeter-wave radio astronomy. *IEEE Transactions on Terahertz Science and Technology*, **2**(6), 593–604. IEEE.
- [92] Su, Y., Yang, J., Zhang, S., Gong, Y., Wang, H., Zhou, X., Wang, M., Chen, Z., Sun, Y., Chen, X., others (2019). The Milky Way Imaging Scroll Painting (MWISP): Project Details and Initial Results from the Galactic Longitudes of 25.° 8–49.° 7. *The Astrophysical Journal Supplement Series*, **240**(1), 9. IOP Publishing.
- [93] Planck Collaboration, et al. (2016). Planck 2015 results. VIII. High Frequency Instrument data processing: Calibration and maps. *Astronomy & Astrophysics*, **594**, A8.
- [94] Baug, T., Wang, K., Liu, T., Tang, M., Zhang, Q., Li, D., Eswaraiah, C., Liu, S.-Y., Tej, A., Goldsmith, P. F., et al. (2020). ALMA observations reveal no preferred outflow-filament and outflow-magnetic field orientations in protoclusters. *The Astrophysical Journal*, **890**(1), 44. IOP Publishing.

- [95] Koch, P. M., Tang, Y.-W., Ho, P. T. P. (2012). Magnetic Field Strength Maps for Molecular Clouds: A New Method Based on a Polarization-Intensity Gradient Relation. *The Astrophysical Journal*, **747**(1), 79. 10.1088/0004-637X/747/1/79, 1201.4263, astro-ph.GA, <https://ui.adsabs.harvard.edu/abs/2012ApJ...747...79K>, Provided by the SAO/NASA Astrophysics Data System.
- [96] Koch, P. M., Tang, Y.-W., Ho, P. T. P. (2012). Quantifying the Significance of the Magnetic Field from Large-scale Cloud to Collapsing Core: Self-similarity, Mass-to-flux Ratio, and Star Formation Efficiency. *The Astrophysical Journal*, **747**(1), 80. IOP Publishing.
- [97] Xu, D., Offner, S. S. R., Gutermuth, R., Kong, S., Arce, H. G. (2022). A Census of Protostellar Outflows in Nearby Molecular Clouds. *The Astrophysical Journal*, **926**(1), 19. IOP Publishing.
- [98] Pattle, K., Lai, S.-P., Di Francesco, J., Sadavoy, S., Ward-Thompson, D., Johnstone, D., Hoang, T., Arzoumanian, D., Bastien, P., Bourke, T. L., et al. (2021). JCMT POL-2 and BISTRO Survey observations of magnetic fields in the L1689 molecular cloud. *The Astrophysical Journal*, **907**(2), 88. IOP Publishing.
- [99] Hwang, J., Kim, J., Pattle, K., Kwon, W., Sadavoy, S., Koch, P. M., Hull, C. L. H., Johnstone, D., Furuya, R. S., Lee, C. W., et al. (2021). The JCMT BISTRO Survey: The Distribution of Magnetic Field Strengths toward the OMC-1 Region. *The Astrophysical Journal*, **913**(2), 85. IOP Publishing.
- [100] Ostriker, E. C., Stone, J. M., Gammie, C. F. (2001). Density, velocity, and magnetic field structure in turbulent molecular cloud models. *The Astrophysical Journal*, **546**(2), 980. IOP Publishing.
- [101] Liu, Junhao, Zhang, Qizhou, Qiu, Keping (2022). Magnetic field properties in star formation: A review of their analysis methods and interpretation. *Frontiers in Astronomy and Space Sciences*, **9**, 943556. Frontiers Media SA.
- [102] Crutcher, Richard M (2004). What drives star formation?. *Astrophysics and Space Science*, 292, 225–237. Springer.
- [103] Kirk, Jason M, Ward-Thompson, Derek, Palmeirim, P, Andre, Ph, Griffin, Matthew Joseph, Hargrave, PJ, Könyves, V, Bernard, J-P, Nutter, David John, Sibthorpe, Bruce, others (2013). First results from the Herschel Gould Belt survey in Taurus. *Monthly Notices of the Royal Astronomical Society*, **432**(2), 1424–1433. The Royal Astronomical Society.
- [104] Thieme, Travis J., Lai, Shih-Ping, Lin, Sheng-Jun, Cheong, Pou-Ieng, Lee, Chin-Fei, Yen, Hsi-Wei, Li, Zhi-Yun, Lam, Ka Ho, Zhao, Bo (2022). Accretion Flows or Outflow Cavities? Uncovering the Gas Dynamics around Lupus 3-MMS. *The Astrophysical Journal*, **925**(1), 32. IOP Publishing.
- [105] Rosolowsky, E. W., Pineda, J. E., Kauffmann, J., Goodman, A. A. (2008). Structural analysis of molecular clouds: dendrograms. *The Astrophysical Journal*, **679**(2), 1338. IOP Publishing.
- [106] Mangum, J. G., Shirley, Y. L. (2015). How to calculate molecular column density. *Publications of the Astronomical Society of the Pacific*, **127**(949), 266–298. The Astronomical Society of the Pacific.

- [107] Frerking, M. A., Langer, W. D., Wilson, R. W. (1982). The relationship between carbon monoxide abundance and visual extinction in interstellar clouds. *Astrophysical Journal*, **262**, 590–605. NASA-supported research.
- [108] Eswaraiyah, C., Li, D., Samal, M. R., Wang, J.-W., Ma, Y., Lai, S.-P., Zavagno, A., Ching, T.-C., Liu, T., Pattle, K., et al. (2020). Unveiling the Importance of Magnetic Fields in the Evolution of Dense Clumps Formed at the Waist of Bipolar H II Regions: A Case Study of Sh 2-201 with JCMT SCUBA-2/POL-2. *The Astrophysical Journal*, **897**(1), 90. IOP Publishing.
- [109] Kauffmann, J., Bertoldi, F., Bourke, T. L., Evans, N. J., Lee, C. W. (2008). MAMBO mapping of Spitzer c2d small clouds and cores. *Astronomy & Astrophysics*, **487**(3), 993–1017. EDP Sciences.
- [110] Terebey, Susan, Shu, Frank H., Cassen, Patrick (1984). The collapse of the cores of slowly rotating isothermal clouds. *Astrophysical Journal*, Part 1 (ISSN 0004-637X), **286**, 529–551.
- [111] Pineda, Jaime E., Segura-Cox, Dominique, Caselli, Paola, Cunningham, Nichol, Zhao, Bo, Schmiedeke, Anika, Maureira, Maria José, Neri, Roberto (2020). A protostellar system fed by a streamer of 10,500 au length. *Nature Astronomy*, **4**(12), 1158–1163. Nature Publishing Group UK London.